

High-Power and Narrow-Linewidth Optimizations of Mid-Infrared Quantum Cascade Lasers

Inauguraldissertation
zur
Erlangung der Würde eines Doktors der Philosophie
vorgelegt der
Philosophisch-Naturwissenschaftlichen Fakultät
der Universität Basel

von

Ilia Sergachev
von Russland

Rieden bei Baden, 2017

Originaldokument gespeichert auf dem Dokumentenserver der
Universität Basel
edoc.unibas.ch

Genehmigt von der Philosophisch-Naturwissenschaftlichen Fakultät
auf Antrag von

Prof. Dr. Stefan Willitsch und Prof. Dr. Jérôme Faist (ETH Zürich).

Basel, 18.04.2017

Prof. Dr. Martin Spiess
Dekan

Abstract

A novel design of high peak power mid-infrared quantum cascade lasers has been modeled, implemented and characterized. Emitting 23.5 W peak power at room temperature, it demonstrated high beam quality, owing to the gain guiding effect, which has not been reported in quantum cascade lasers before.

A new concept of constant power laser current source has been proposed and designed in a circuit performing reduction of optical frequency noise by reducing the amount of the electrical power fluctuations generated by the laser itself. Significant reduction of optical frequency noise has been measured without locking the laser frequency to any optical reference.

Quantum cascade lasers operating at two frequencies simultaneously have been characterized in terms of frequency stability. A high value of correlation observed between instant frequencies of the two modes allowed to implement a scheme with indirect frequency locking, where the mode not locked to an optical reference experienced frequency noise reduction while the other one was used for stabilization.

Acknowledgements

In the first place I would like to profoundly thank my excellent supervisors – Dr. Richard Maulini and Professor Dr. Stefan Willitsch, for all the guidance they provided the best way possible. I would also like to thank Professor Dr. Jérôme Faist for kindly agreeing to review my work.

It was a pleasure to work with all the colleagues in Alpes Lasers, University of Basel and University of Neuchâtel – I am grateful to them for their help and my experience.

I am deeply grateful to all my teachers – for their patience and for giving me the pleasure of discovering new things.

I thank my parents, grandparents and Lena – for all the freedom and love they are giving me.

This work I did within the COMIQ Marie Curie Initial Training Network. It was an honor to be a part of this network; I thank all its members and especially Michael and Celia for the mindful coordination.

Table of Contents

Abbreviations

1	Introduction	1
1.1	Quantum Cascade Lasers	1
1.2	Motivation and applications	4
2	High power	7
2.1	QCL power and beam quality	7
2.2	Gain guided quantum cascade lasers	12
2.2.1	Principle of operation	12
2.2.2	Simulations	12
2.2.3	Fabrication	18
2.2.4	Methods and experimental results	19
2.3	High power pulsed driver	28
2.4	Conclusions	32
3	Narrow linewidth	33
3.1	Linewidth and frequency noise	33
3.2	Measuring the optical frequency	37
3.3	Stabilization and noise reduction	40
3.4	Frequency noise in QCLs	42
3.5	Constant power laser driver: digital implementation	45
3.5.1	The design idea	45

3.5.2	Experimental setup	47
3.5.3	Calibration	49
3.5.4	Results	49
3.6	Constant power laser driver: analog implementation .	53
3.6.1	Motivation	53
3.6.2	Low noise constant current source	55
3.6.3	Design and simulations	55
3.6.4	Characterization	61
3.6.5	Results	65
3.7	Conclusions on power stabilization	71
3.8	Dual frequency QCLs	72
3.8.1	Introduction	72
3.8.2	Laser fabrication	73
3.8.3	Characterization	75
3.8.4	Stabilization	80
3.8.5	Conclusions	83
4	Conclusions	85
Bibliography		87
Appendix A	Probe for RF measurements	108
Appendix B	Measurement of frequency tuning	111
Appendix C	Beam collimation	113
Appendix D	Tools	115

Abbreviations

ADC	Analog to Digital Converter
CW	Continuous Wave
DAC	Digital to Analog Converter
DBR	Distributed Bragg Reflectors
DFB	Distributed Feedback
DIRCM	Directional Infrared Counter Measures
FFT	Fast-Fourier-Transform
FNPSD	Frequency Noise Power Spectral Density
FPGA	Field-Programmable Gate Array
FSR	Free Spectral Range
FTIR	Fourier Transform Infrared Spectroscopy
FWHM	Full Width at Half Maximum
FWM	Four Wave Mixing
HHL	High Heat Load
ICW	Intermittent Continuous Wave
IV	Current-Voltage
LEF	Linewidth Enhancement Factor

LIDAR Light Detection And Ranging
LIV Light-Current-Voltage
LLH Laboratory Laser Housing
MCT Mercury Cadmium Telluride
MOSFET Metal-Oxide-Semiconductor Field-Effect Transistor
NA Numerical Aperture
PDH Pound-Drever-Hall
PI Proportional-Integral
PZT Piezoelectric Transducer
QCL Quantum Cascade Laser
RF Radio Frequency
RMS Root Mean Square
SHB Spatial Hole Burning
SPICE Simulation Program with Integrated Circuit Emphasis
TE Transverse Electric
TEC Thermoelectric Cooler
THz Terahertz
TM Transverse Magnetic
ULE Ultra-Low Expansion
WPE Wall-Plug Efficiency

1

Introduction

1.1 Quantum Cascade Lasers

The principle of operation of a *Quantum Cascade Laser* (QCL) was proposed in 1971 [1] and realized in 1994 [2]. Since then, they have enabled the development of many applications requiring mid-infrared to *Terahertz* (THz) light. The heart of a QCL is a sequence of quantum wells, called active region, which is physically implemented in ultra-thin epitaxial layers of semiconductor materials. In contrast to the usual interband semiconductor lasers, where light is emitted during the recombination of electrons and holes between the conduction and valence bands, QCLs are based on intersubband transitions – therefore only the electrons in the conduction band participate in the emission of light. This defines the two principal features of QCLs:

- Because the energy levels between which the lasing transitions occur are defined by the depths of quantum wells, the emission wavelength can be adjusted via the layer thicknesses – in contrast to the interband lasers, where the energy levels are mostly defined by a combination of materials.
- As no recombination is involved, the same electron can be reused

for emission multiple times, passing through *cascaded* sequences of quantum wells. This is widely used in order to increase the efficiency and output powers by stacking tens of such – at a price of an increased operation voltage.

An example of one period of an active region of a THz QCL is shown in Figure 1.1. In the original research 180 of such were stacked to obtain 1 W of optical output power in the 3.4 THz wavelength range [3].

An epitaxially grown, few μm thick active region structure is then usually shaped into one of the two common forms of optical waveguides, called *ridge* and *buried heterostructure* (Figure 1.2), and pumped with electrical current [4].

Numerous properties of QCLs can be successfully engineered nowadays. In terms of wavelength, QCL designs were demonstrated between 2.6 μm (115 THz) and 250 μm (1.2 THz) [7, 8]. Depending on the spectral selectivity of the waveguide or external optical feedback elements, QCL emission can be from narrow linewidth single mode [9] to an octave spanning periodic set of modes [10]. Intrinsic nonlinear effects can be employed additionally to achieve frequency comb operation [11]. Spectral tuning of QCL emission is easiest to achieve thermally – thus varying the effective refractive index of its waveguide: changing either external heatsink temperature (slower and wider), or the pumping current (faster and narrower). Embedded microheaters were demonstrated recently to add even more flexibility in tuning [12]. Much larger coverage of the gain curve of a given active region structure is obtained by an external mechanically adjustable grating [13] at the cost of increased system size and higher sensitivity to environmental conditions – such as vibration and changes of temperature.

A typical mid-infrared QCL reaches tens of milliwatts of output power with around 10% *Wall-Plug Efficiency* (WPE) . This can then be optimized to 5 W of *Continuous Wave* (CW) power [14, 15] or over 200 W of peak power in the pulsed case [16]. However, for the reasons,

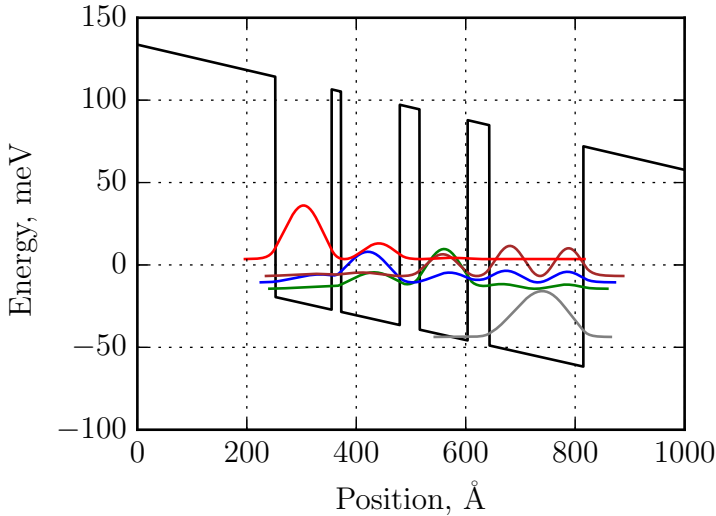


Figure 1.1: The simulated electronic band structure of one gain stage of a THz QCL. The black curve represents a sequence of quantum wells, the colored ones – the electron probability density of different electron states. Such a stage enables an emission of one photon per each electron passing through it; such a pattern is usually repeated numerous times within an active region. The simulation performed using QWWAD software [5, 6] with the structure data taken from [3].

described in section 2.1, power scaling in QCLs is not trivial and often requires efforts to maintain beam quality at an acceptable level.

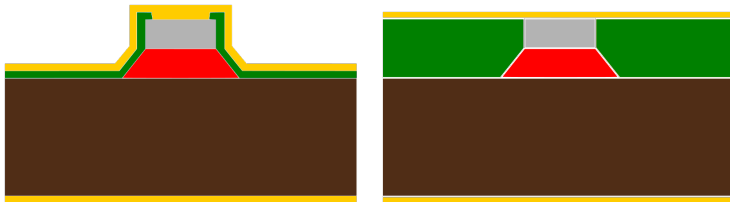


Figure 1.2: Schematic representations of cross-sections of QCLs with a ridge waveguide (left) and a buried heterostructure one (right). Red is the active region; brown is the substrate; grey is the top cladding; green is the electrical insulation; yellow are top and bottom contacts. The electrical current is flowing in the vertical direction; the emitted light is propagating in the direction normal to the drawing.

1.2 Motivation and applications

Even though one can not make a single laser ideal in every aspect, a number of its properties can be improved simultaneously for a certain application. In terms of stability of optical frequency and CW output power, one of the challenging applications for mid-infrared sources and QCLs in particular is precision spectroscopy of cold molecules [17].

Values of fundamental physical constants (for instance, the proton-to-electron mass ratio $\mu = m_p/m_e$) can be improved in precision by measuring frequencies of weak electric-dipole forbidden transitions in cold molecular ions [18]. In this first of its kind experiment for exciting the two spectral lines of N_2^+ at 2186.173 and 2186.180 cm^{-1} a commercial single-mode external cavity QCL was used, delivering 170 mW of optical power and 30 MHz of linewidth. In the end, this linewidth was the limitation of precision for the experimental results: for proper spectroscopy of Doppler-broadened transitions as in those experimental conditions laser should have been better than 1 MHz. Natural linewidths of such transitions are expected to be in nanohertz range [19], leaving plenty of room for improvement for the light source which would be exciting them in future experiments.

Similarly, precise measurements of the m_p/m_e ratio (and its possible variation over time) can be performed via two-photon vibrational spectroscopy of H_2^+ in the 9.2 μm wavelength range [20–22] – requiring the linewidth of a probing laser to be in the kHz range. Such wavelengths are easily accessible for QCLs, but their free-running linewidths are typically few orders of magnitude as high, i.e. in the MHz range. Therefore, in these works, a scheme involving phase-locking a QCL with a tunable frequency offset to a stable CO_2 laser as an absolute reference was used in order to perform the high resolution spectroscopy. Other electric quadrupole transitions of H_2^+ around 4.6 μm and 4.8 μm are proposed in [23].

At 8.6 μm , line centers of two-photon ro-vibrational transitions of CHF_3 [24, 25] can be measured by narrow linewidth QCLs for the same fundamental purpose. In this case authors have used optical feedback from a high-finesse V-shaped cavity in order to narrow down the linewidth of a QCL observed during 1 ms below 4 kHz.

Another target for high resolution spectroscopy at 6.2 μm can be MgH^+ [26].

The laser power is important for such experiments besides the frequency stability: the weakness of the measured transitions means a low probability to excite them – therefore, the higher the number of photons available, the shorter is the observation time required. Essentially, a high beam quality is necessary to be able to focus the beam tightly on a microscopic Coulomb crystal or couple it efficiently into a high-finesse optical resonator.

Furthermore, applications such as *Light Detection And Ranging* (LiDAR) [27] and *Directional Infrared Counter Measures* (DIRCM) [28] support the demand of development of high power and excellent beam quality mid-infrared lasers.

Motivated by those applications, this work is focused on high power and low optical frequency noise optimizations of quantum cascade lasers. As limits for them are in different physical effects, they can be addressed independently, but the results obtained in both directions

can be merged in further works.

2

High power

2.1 QCL power and beam quality

The structure of a typical mid-infrared QCL can be considered as an active region with dimensions of $3\text{ mm} \times 2\text{ }\mu\text{m} \times 10\text{ }\mu\text{m}$ (which are cleaved cavity length, its thickness in the growth direction, and width etched during the fabrication), surrounded by electrically insulating claddings on the sides and conductive ones on top and bottom. The WPE of under 30% [29–31] and the combined thermal conductance in the vertical and horizontal directions of the surrounding layers allowing the removal of several watts of generated heat load give an idea about the maximum value of CW output power demonstrated by now – a few watts [14, 15].

In the questions of scaling of the output power and optical beam guiding, QCLs can be compared to semiconductor diode lasers, which employ similar waveguide geometries and can share some working solutions due to being longer on the market and better developed. However, several important effects distinguish QCLs and have to be considered:

1. Compared to the diode lasers, which can operate in both *Trans-*

verse Electric (TE) and *Transverse Magnetic* (TM) polarizations, QCLs can only support the second one. As their light generation is based on intersubband transitions, only the electric field in the growth direction of a laser structure can be amplified due to the quantum mechanical selection rules [4, 32]. This property allows, for instance, making lasers with a tilted front facet, which selectively reduces the TM reflectivity, thus improving output power and slope efficiency [33]. Furthermore, in the TM case, a specific solution in a form of a bound mode, called interface plasmon mode, exists for a dielectric waveguide if at some interface inside of it there is a change of the sign of the real part of the dielectric constant. This, in fact, is a usual situation for QCLs, as top electrical contact is done by surface metallization. Solutions based on plasmon modes were employed both for making long wavelength QCLs [34, 35] and controlling the mode guiding in the mid-infrared ones [36]. As a downside, if no special precaution is taken, because of the TM polarization facet reflectivity increases with mode order [37] and broad area QCLs lase on a high-order mode with a far field profile consisting of 2 lobes propagating at large angles from the optical axis [38, 39].

2. The *Linewidth Enhancement Factor* (LEF) of QCLs, which is responsible for the coupling between amplitude and phase of the optical field, is close to zero [40, 41]. It has been shown, that LEF is an important factor causing random filamentation instability (random formation of narrow regions with local maxima of current and photon density) in diode lasers [42, 43] when wide waveguides are used for the power scaling [44]. However, in wide (broad area) QCLs, due to the low LEF, such an effect has not been observed [38, 45].
3. The nonlinear effects such as *Four Wave Mixing* (FWM) [46] and *Spatial Hole Burning* (SHB) [47], which are usually insignificant

in standard semiconductor lasers, play important roles in multimode behaviour of QCLs owing to picosecond-fast electronic transport and gain recovery [48]. For instance, in QCLs wide enough to operate in more than one transverse mode, FWM has been proven to cause coherent coupling of multiple transverse modes and the resulting beam steering [49]. SHB, on the other hand, reduces the stability of lasing of a QCL in a single standing mode of its resonator, by favoring other longitudinal and transverse modes (thus causing spectral broadening and beam steering) [47, 50].

An obvious direction to increase the output power of a QCL is to enlarge the volume of its active region. While the chip length is limited to ≈ 10 mm by practical reasons of fabrication and packaging, successful scaling in the other two dimensions has been demonstrated. In the vertical (epitaxial growth) direction the increase of number of gain stages leads to the increase of quantum efficiency (number of photons generated by each electron), thus peak output power [51]. In the horizontal direction the widening of the active region provides similar nearly linear scaling of the peak output power [38]. However, in both cases the concomitant increase of heat dissipation limits the average output power. In order to overcome this, a 30 μm wide QCLs with only 10 cascades in the active region lasing in CW regime up to +100 °C [52] was demonstrated recently. In this configuration, only vertical heat flow from the active region was employed, so, in principle, it opens a path to further scaling of ridge width for higher average output powers.

The problem that arises after exceeding the characteristic width or height of a waveguide equal to emission wavelength is the degradation of beam quality. It happens because larger waveguides support not only the fundamental optical mode, but also the higher order ones; in this case, as mentioned above, the TM polarization and nonlinear effects can significantly favor them. Beam quality is important for many applications – whenever light needs to be focused at large

distance – e.g. remote sensing and countermeasures, or efficiently coupled into optical elements (fibers, resonators, nonlinear crystals etc). A typical mid-infrared QCL has good beam parameters (beam propagation factor [53] $M^2 < 2$), but, due to the waveguide dimensions close to the operating wavelength, has significant beam divergence [54] (for example, in the cited work, the wavelength is $8.77\text{ }\mu\text{m}$, the active region thickness and width are $\approx 2.1\text{ }\mu\text{m} \times 15\text{ }\mu\text{m}$, resulting in $62^\circ \times 32^\circ$ FWHM divergences). Therefore, in order to collimate it efficiently and without distortion, a high *Numerical Aperture* (NA) lens needs to be carefully aligned in front of it (for example, Figure 2.1 shows a high power QCL chip packaged with a collimating NA = 0.85 aspheric lens). A bad example of beam collimation faced during this work is shown in Appendix C.

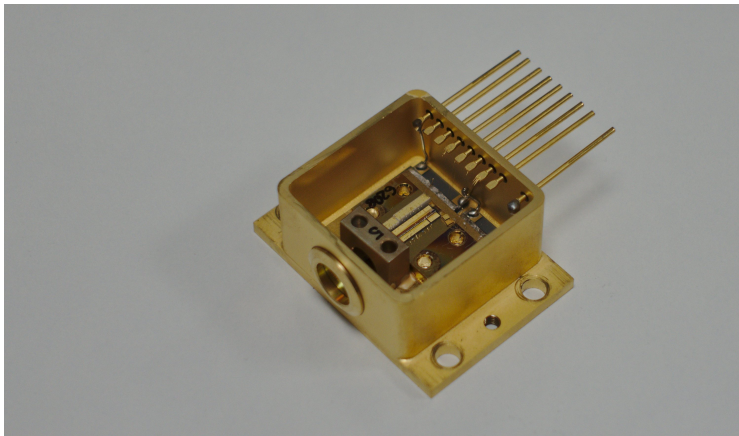


Figure 2.1: A high power QCL chip mounted in a sealable *High Heat Load* (HHL) housing (top lid removed for illustrative purpose) together with a collimating aspheric lens inside its mount labelled '5' and temperature sensor on top of a *Thermoelectric Cooler* (TEC) .

Several approaches altering the simplest dielectric waveguide attempt to overcome the problem of the emergence of high order optical modes in QCLs with large waveguides.

- Angled cavity [16], being relatively easy to implement, allows to improve significantly the output beam shape of a 300 μm wide QCL making it single lobed after a careful choice of the tilt angle. An impressive peak power of 203 W has been demonstrated with this approach, though still not with a perfectly gaussian beam shape ($M^2 \approx 4$).
- Lasers can be placed carefully side-by-side in an antiguide array with a subwavelength lateral separation [55] in order to obtain resonant leaky-wave coupling [56] and in-phase lasing from the whole combined facet of the array. Compared to a simple wide-ridge laser with the same effective width (105 μm in the cited work), the antiguide array configuration allows to obtain a near-diffraction-limited output beam together with a reasonably high peak power (5.5 W at room temperature).
- The Talbot effect [57] has been employed in diode lasers [58] and QCLs [59, 60] to couple diffractionally arrays of adjacent lasers by forming a common cavity, and provide controllable discrimination of lateral modes. The phase-locked operation of QCL arrays produced this way allows to scale the peak output power nearly linearly (e.g. a total of 4 W from 6 lasers [60]), though still requiring further work to make the output beam single-lobed.
- Photonic crystal gratings are often found to be prominent not only to control the shape of the laser beam of broad area lasers, but also their spectral properties – for example, to make single frequency lasers [61, 62]. 12 W peak powers in nearly diffraction-limited beams have been demonstrated [63]. Combined with deep etching and further regrowth with thermally conductive materials, this is believed to improve the heat extraction and lead to high power, single mode and good far field QCLs [64].

2.2 Gain guided quantum cascade lasers

2.2.1 Principle of operation

In the present work, high peak power at room temperature has been achieved together with high beam quality.

For this, an unusual waveguide design was implemented: the active region was not etched after growth – only a cladding above was. This created a very wide active region compared to standard QCL designs and a narrow current injector on top. Therefore, the current distribution in the active region became strongly non-uniform with a decay from the laser center to its sides. As the active region was not etched, the usual optical mode confinement by a refractive index step in the horizontal direction was eliminated. Instead, the gain profile corresponding to the horizontal current density spread led to gain guiding (i.e. confinement of the optical field in the central part of the waveguide, where the gain was high [65]) and efficient optical mode selection.

2.2.2 Simulations

The effect of gain guiding was accurately simulated numerically¹. One symmetric half of a 2D cross-section of a QCL waveguide was used in all simulations with layer geometries corresponding to the ones in fabricated devices – see Figure 2.2 and subsection 2.2.3 for details. It is important to emphasize that the depth of etching was not known precisely after fabrication; therefore, it was used as a fitting parameter. Simulations with different values of the etching depth demonstrated the scaling of the width of the distribution of the current density without changing the magnitude of this distribution (Figure 2.3 and the inset of Figure 2.4), and no qualitative changes in device physics. A value of 7 μm , which corresponds to 1 μm of cladding thickness left

¹ Most of the simulations have been performed with the COMSOL Multiphysics software including the Wave Optics module.

unetched, was found to make the closest match between simulated and experimental data and therefore was used. Values for the refractive index and the conductivity of the materials were taken from [66] and [67]. No change in simulated laser properties was observed while varying the current injector width from 8 to 16 μm ; the result for a value of 10 μm is shown in Figure 2.2.

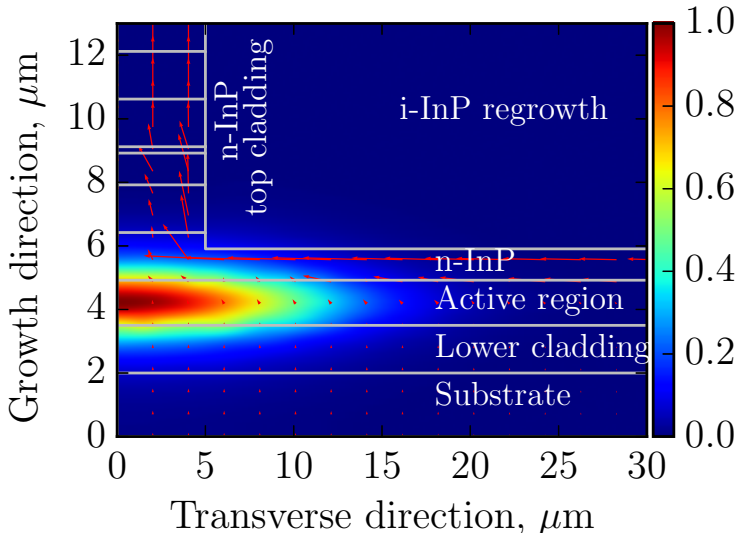


Figure 2.2: Simulated fundamental optical mode intensity (color, a.u.) and current flow (red arrows) in the center of a cross-section of a gain-guided laser (one transverse symmetric half is shown). The applied voltage is 20 V.

First, the current density distributions in the whole cross section were calculated for a range of voltages applied between the top and bottom contacts. For an active region much wider than in the conventional index-guided QCLs, the current density could not be assumed uniform anymore, and the local dependence of the conductivity in the growth direction on the electric field was accounted for. This dependence was

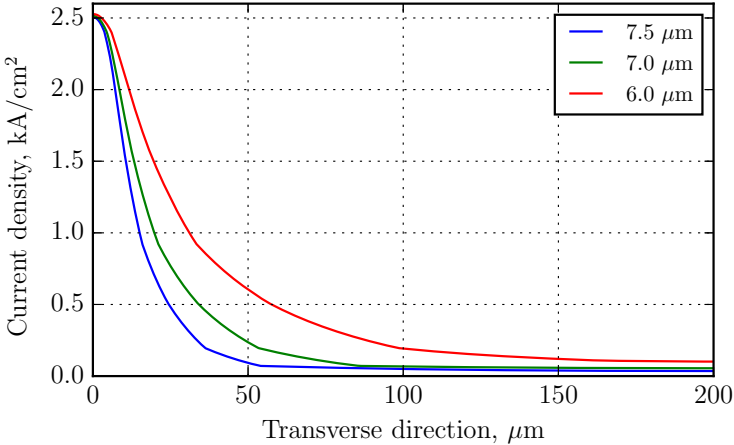


Figure 2.3: Simulated current-density lateral distribution in the active region of a gain-guided QCL as a function of the etching depth (one transverse symmetric half is shown). The applied voltage is 16 V.

obtained experimentally, as proposed in [68], from a standard measurement of a *Current-Voltage* (IV) curve of a narrow ridge device with the same active region design, where the current density is uniform; similar to [68], the conductivity of the active region in the lateral direction was taken as a weighted average of the bulk ones of its layers. Even though the non-uniform conductivity added the complication of a cyclic dependence of the input variable (conductivity) on the output solution (electric field) for the numerical solver, the solution still converged. The distributions of the current density in the active region for a set of applied voltages are shown in Figure 2.4. They were integrated over horizontal cross section of the model (e.g. $y = 0$ plane in Figure 2.2) in order to obtain full current through the device at each applied voltage and simulate the IV curve (Figure 2.5).

Second, the distributions of the gain as a function of the current density were calculated for each applied voltage. The gain function was simulated according to [69].

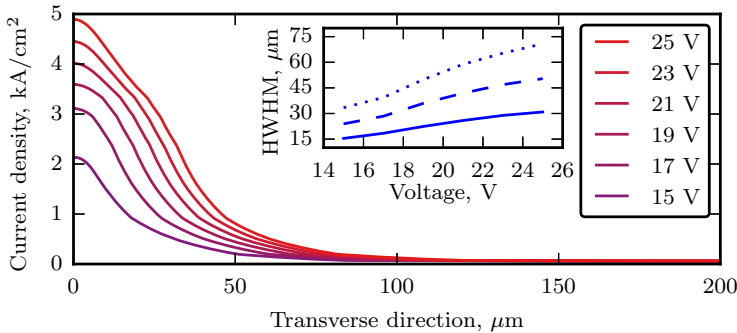


Figure 2.4: Simulated current-density lateral distribution in the active region of a gain-guided QCL as a function of the applied voltage (one transverse symmetric half is shown). Inset: half width at half maximum (HWHM) of the current density distribution as a function of the applied voltage (solid curve) for 1 μm of cladding thickness left unetched as in fabricated devices. Simulations for 2 μm (dashed curve) and 3 μm (dotted curve) provided for comparison as well.

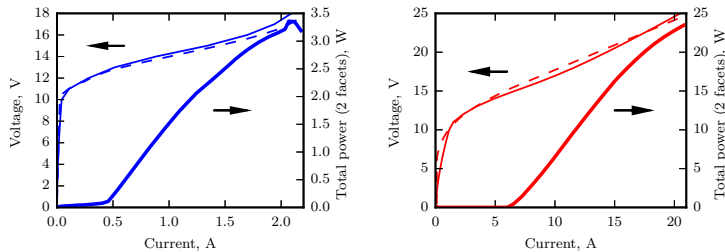


Figure 2.5: LIV curves for an index guided laser (left) and a gain guided laser (right) at 20°C, 300 ns pulse width, 1% duty cycle. Bold lines – measured power, thinner lines – measured voltage, dashed – simulated voltage.

Third, a boundary electromagnetic mode analysis² was conducted for each distribution of the gain, accounting for the refractive indices of the layers as well. For all voltages > 16 V, the TM00 mode is effectively confined by the gain distribution and its imaginary refractive index is higher than for TM01³ which indicates, that it also reaches the lasing threshold first (Figure 2.6). Higher-order modes have negative net gain (= losses) in this simulation. An example of mode electric field intensity is shown in Figure 2.2. The role of the gain guiding was proven by running an additional simulation of the same device geometry without gain variation: this resulted in high order mode operation. However, if then the etching-depth parameter was increased to reproduce the usual QCL geometry with an etched active region (Figure 2.7), horizontal index guiding and zero-order-mode favoring were observed again as expected, which became an additional proof of reliability of our model. A more precise model should have included the thermally induced variation of the refractive-index profile during the current pulse – that, however, would dramatically increase the complexity of simulations.

Finally, at 20 V applied voltage (corresponds to ≈ 14.3 A) the far-field intensity profile of the laser was calculated based on the mode-intensity distribution in the cross section. A single gaussian-like lobe with 56° vertical and 8° horizontal full angles of divergence was obtained. While the vertical angle was usual for a QCL [54], the horizontal one was few times smaller, which corresponded well to the stretched mode shape in the waveguide (Figure 2.2), and what was observed later experimentally.

² Solving using the effective index method [70] the time-harmonic Maxwell's equations for the out-of-plane propagation constant.

³ Strictly speaking for such a complicated waveguide the modes should be named quasi-TM00 and quasi-TM01 [70], but for the simplicity they will be called TM00 and TM01 [71].

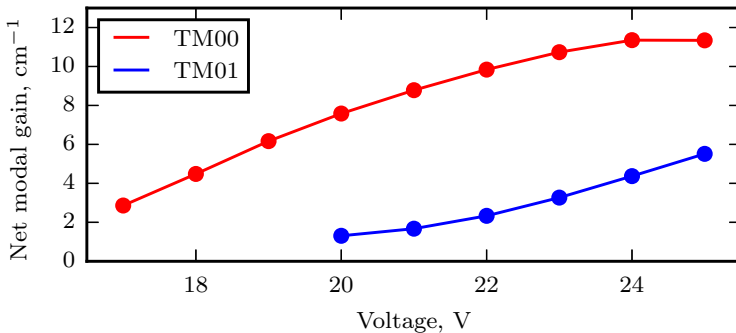


Figure 2.6: Simulated modal gain as function of applied voltage in a gain-guided QCL. The high gain margin between the TM00 and TM01 modes makes the TM00 always reach lasing threshold first.

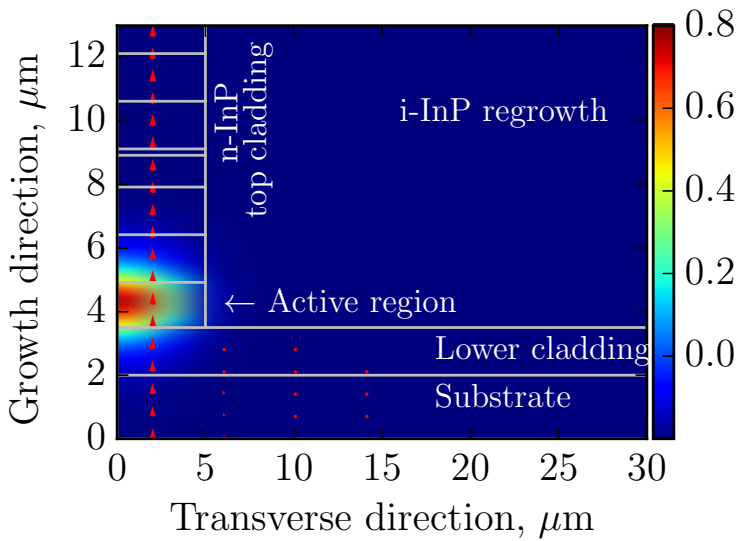


Figure 2.7: For comparison: an index-guided QCL structure simulated with a larger ($9 \mu\text{m}$) etching depth using the same model.

2.2.3 Fabrication

The QCL active region and top cladding were grown in a multi-wafer molecular beam epitaxy (MBE) reactor in a single growth step on n-doped substrates (InP:S, $n \approx 1 - 4 \times 10^{17} \text{ cm}^{-3}$). The growth started with a 1.5 μm -thick, low-doped InP layer (Si dopant, $n = 3 \times 10^{16} \text{ cm}^{-3}$). The active region consisted of 35 stages (total thickness: 1.42 μm) of a strain-balanced $\text{In}_{0.71}\text{Ga}_{0.29}\text{As} / \text{Al}_{0.75}\text{In}_{0.25}\text{As}$ (strain: +1.18%/-1.86%) two-phonon-resonant design [72] with a sheet carrier density per stage of $4.86 \times 10^{10} \text{ cm}^{-2}$. The upper cladding layer sequence, grown with MBE, from bottom to top was: InP (Si, $3 \times 10^{16} \text{ cm}^{-3}$) 1.5 μm , InP (Si, $1 \times 10^{17} \text{ cm}^{-3}$) 1.5 μm , InP (Si, $8 \times 10^{18} \text{ cm}^{-3}$) 1.0 μm , InGaAs (Si, $2 \times 10^{19} \text{ cm}^{-3}$) 0.2 μm .

After growth, one of the wafers was processed in ridge-waveguide (RWG) configuration with a ridge width of 12 μm for cw operation using dry etching to obtain vertical sidewalls and a thick gold deposition by electro-plating for improved heat dissipation. The results obtained with this wafer were used as a reference point to evaluate the performance of the gain-guided devices.

Another wafer from the same epitaxial growth was processed in a gain-guided broad-area laser configuration using a process based on the one described in [73]. The upper cladding thickness was increased by growing with metal-organic chemical vapour deposition (MOCVD) the additional 4 μm of layers of InP (Si) with doping concentrations increasing from $2 \times 10^{16} \text{ cm}^{-3}$ at the bottom to $1 \times 10^{19} \text{ cm}^{-3}$ at the top (layers between 9 and 13 μm of vertical axis on Figure 2.2). Then the narrow current injection region was formed by etching highly conductive top cladding layers with a wet solution of HBr/HNO₃/H₂O and regrowing the insulating InP:Fe. Several different current injector widths between 10 and 16 μm were fabricated on the same wafer; this parameter variation did not affect laser performance. $\approx 1 \mu\text{m}$ of the low-doped ($3 \times 10^{16} \text{ cm}^{-3}$) cladding layer has been left (corresponding to 7 μm etching depth mentioned in subsection 2.2.2). The resulting device geometry corresponded to the one simulated (Figure 2.2).

Both narrow-ridge-waveguide and gain-guided QCLs were cleaved in 6 mm-long chips and mounted epitaxial-side up on Cu carriers with In solder (Figure 2.8). Facets were left as cleaved.

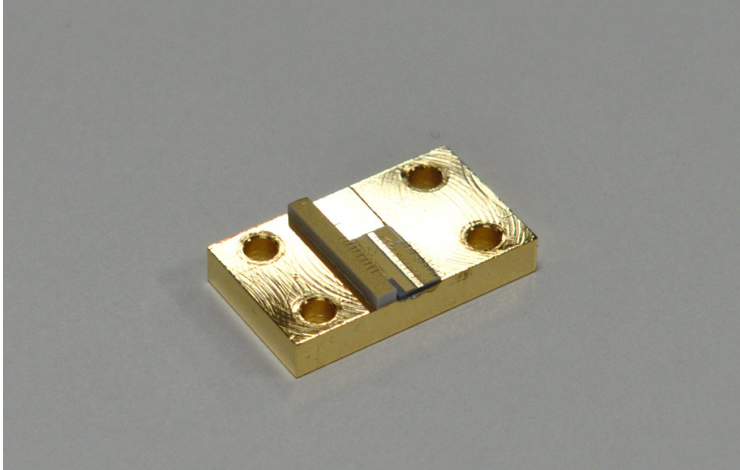


Figure 2.8: A 6 mm-long gain guided QCL chip mounted epi-side up on a copper submount.

2.2.4 Methods and experimental results

All the measurements were taken at room temperature (20°C) with 300 ns pulse width and 1% duty cycle (i.e. 30 μs pulse period) unless otherwise stated. Standard *Light-Current-Voltage* (LIV) curves are shown in Figure 2.5. The peak power of a gain guided device reached 23.5 W at 20.4 A (limited by electronics, as laser rollover was not reached), which is over 7 times as large as the maximum power of an index-guided one at its rollover. A 300 ns pulse width was chosen as an optimal value so that, on the one hand, measurements were not affected by ≈ 5 ns rise/fall times, and on the other hand power was not reduced by heating. However, no change of LIV curves was ob-

served for pulse widths between 60 ns and 600 ns. The WPE at these conditions reached 11% at 1.2 A for the index guided and 5.5% at 14 A for the gain guided lasers. The lower value for the gain guided configuration is explained by the non-uniform lateral distribution of the pumping current: while creating the necessary effect of gain guiding, it also makes the value of the current density close to optimal for WPE only in the center of the active region, and leaves large further outlying parts of it driven with sub-optimal and even sub-threshold currents. A further improvement of this design could attempt to remove the tails of the current distribution in a configuration with an optimally etched active region, which would be still wide enough to benefit from the gain guiding.

At 20% duty cycle the averaged total power emitted by the gain guided device reached a maximum of 1.6 W. Cooling the lasers down to -30°C led to the power increase by 22% for the index-guided and by 40% for the gain-guided lasers compared to room temperature operation. A typical measured emission spectrum of the fabricated lasers is shown in Figure 2.9.

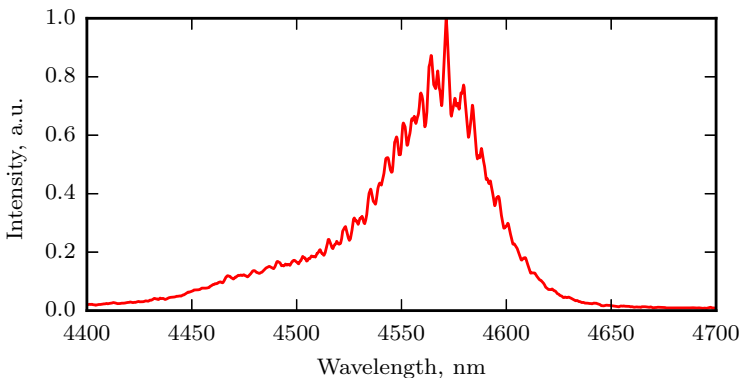


Figure 2.9: Typical measured emission spectrum of a gain-guided laser.

The output beam was characterized using a pyroelectric camera with

a 124×124 pixel, $100 \mu\text{m}$ pitch focal plane array (FPA) and a mechanical chopper. The camera was first placed 6 mm away from the laser facet to characterize the overall beam shape and check for the presence of side lobes. In this configuration, the FPA covered an angular range of $90^\circ \times 90^\circ$ with a resolution of 0.95° . Four beam pictures taken at various currents I between $1.2 \times I_{th}$ and $3.4 \times I_{th}$ are shown in Figure 2.10 ($I_{th} \approx 6 \text{ A}$ – current of the lasing threshold for the gain-guided lasers (Figure 2.5)). The duty cycle of current pulses defined above had to be lowered from 1% to 0.5% when reaching $1.9 \times I_{th}$ and then to 0.4% when reaching $3.4 \times I_{th}$ in order not to saturate the camera sensor. As can be seen, the beam consisted of a single bell-shaped lobe centered on the optical axis. In contrast to index-guided broad area QCLs [38] and phase-locked QCL arrays [55], no lateral lobes propagating at large angles from the optical axis were observed. Furthermore, the beam retained its well-behaved shape up to the maximum current $I_{max} = 3.4 \times I_{th}$.

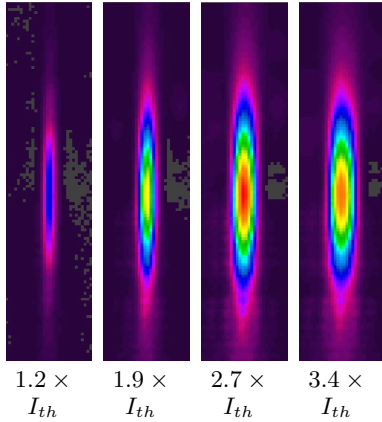


Figure 2.10: Measured beam intensity profiles of a gain-guided QCL at a distance of 6 mm for various injection currents. Each image dimensions are $3.0 \times 12.4 \text{ mm}^2$ (initially $12.4 \times 12.4 \text{ mm}^2$, sides containing no signal were cropped).

After confirming the absence of side lobes, the camera was positioned 24 mm away from the output facet, in the far field of the laser, to measure the beam divergence. The intensity values measured by the individual camera pixels were summed column by column and fitted with a gaussian line shape to determine the horizontal beam diameter (Figure 2.11). Excellent agreement between the measured profile and the gaussian fit function was observed up to $2.5 \times I_{th}$. Above this value, the beam shape started to deviate from gaussian but remained single-lobed without dips. One of the reasons for that could be the thermally induced non-uniform increase of the refractive index, which is stronger at higher currents and better confines the modes, including higher order ones. In addition, when the electric field in the active region equals and then exceeds the resonant tunneling condition, the optical gain saturates and then decreases with increasing current density because most carriers are not injected into the upper laser level. This leads to a flattening of the gain spatial profile and then in the emergence of a dip in the middle of the waveguide resulting in a weaker guiding of the fundamental mode.

The beam propagation factor M^2 was measured by collimating the beam with an aspheric lens ($f = 1.873$ mm) and measuring the beam second moment width at different distances with the same camera. In the vertical direction, $M_y^2 = 1.271 \pm 0.003$ which is typical for QCLs [54]. However, in the horizontal one the precise measurement could not be obtained with the available optics due to the strong ellipticity of the beam, and a value $M_x^2 \approx 6$ could be estimated.

Additionally, the time evolution of far field profile of the beam was measured by capturing the intensity variation at maximum current with a fast optical detector as a function of the horizontal angle of observation (Figure 2.12). The distance from the laser facet to the detector was 75 mm. The detector signal was captured with a fast oscilloscope synchronized with the laser pulse driver. It is clearly visible that after the first ≈ 40 ns of the pulse, where laser was operating in a pure fundamental mode, higher order modes started to contribute,

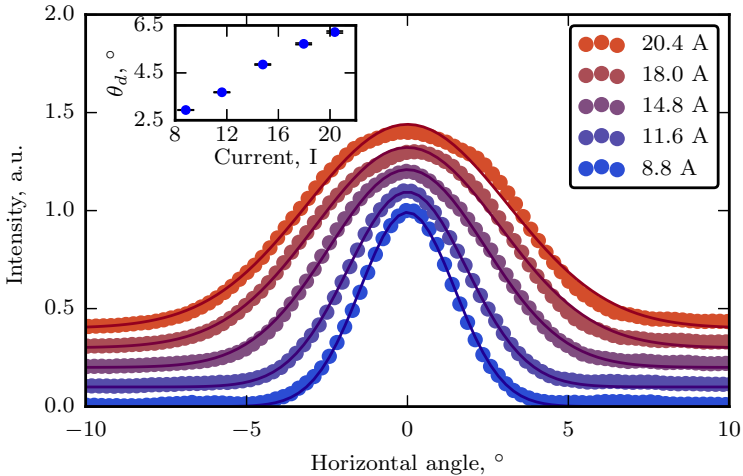


Figure 2.11: Measured horizontal far-field intensity profile of a gain-guided QCL at various currents (dots) along with gaussian fits (lines). Curves are shifted vertically with a step of 0.1 for distinctness. Inset: half angle beam divergence (θ_d) at $1/e^2$ of the maximum value extracted from gaussian fits with black error bars representing one standard deviation.

which resulted in beam steering and widening. This explains a rather high value of the measured M_x^2 . Nevertheless, the laser output averaged over time, like, for example, with camera measurements described above, remained gaussian-like single-lobed. Moreover, this lateral mode hopping behaviour has demonstrated a perfect pulse-to-pulse repeatability and high stability to variations of current and heatsink temperature. At lower currents, the same pattern of beam variation was observed, but more stretched proportionally along the time axis (i.e., the variation was slower). In particular, the observed operation time in the fundamental mode at the pulse start (0 – 40 ns in Figure 2.12) was longer. The observed behaviour can have few possible reasons: as mentioned above, it can be caused by thermal index guiding [74] or distortion of the gain spatial profile. As indicated in Figure 2.13 and Figure 2.14, a 300 ns long 25 V electrical pulse

leads to a temperature rise of at least 80 K in the center of the active region, therefore a significant temperature contrast, which induces a lateral variation of refractive index due to the thermo-effect. A future improvement of the gain guiding simulations presented in subsection 2.2.2 could include this index profile variation in a time-resolved manner. Other than that, similar far field intensity distributions in broad area QCLs have been attributed to the coherent coupling of few transverse modes due to four-wave mixing [49].

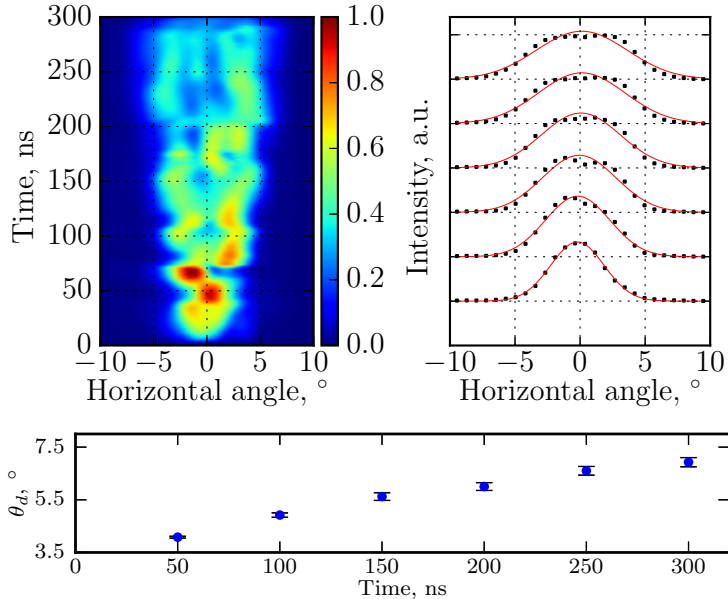


Figure 2.12: Top left: measured instantaneous horizontal far-field intensity evolution (color, a.u.) of a gain-guided QCL during a 300 ns pulse at a maximum current of 20 A showing a transition from the fundamental mode to the higher order ones. Top right: same data averaged within time intervals from 0 ns to a given time (from bottom to top: 50 ns, 100 ns, 150 ns, 200 ns, 250 ns, 300 ns) shown with black dots along with gaussian fits (red lines). Bottom: half angle beam divergence (θ_d) at $1/e^2$ of maximum value extracted from gaussian fits with black error bars representing one standard deviation.

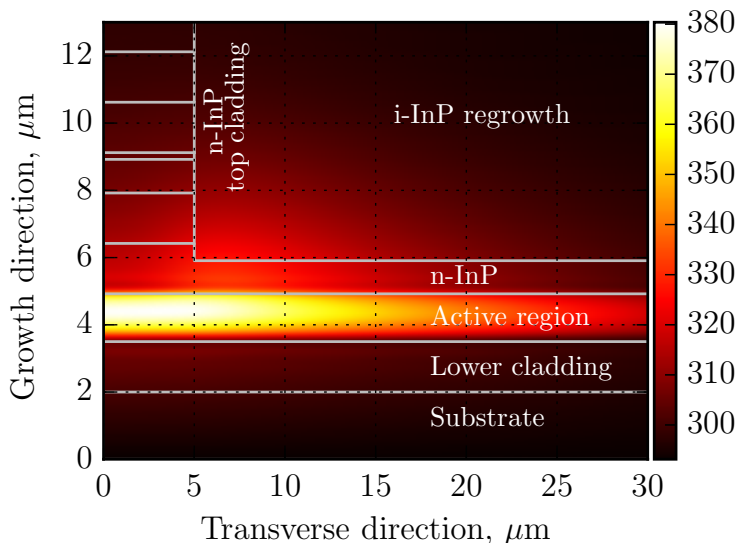


Figure 2.13: The simulation of the temperature distribution in the center of a gain guided QCL after 300 ns of a 25 V electrical pulse. Color: temperature, K. The initial temperature distribution at $t=0$ ns is uniform with 293 K everywhere. The heatsink temperature of 293 K is kept constant at the bottom surface ($y=0$ μm plane). One transverse symmetric half is shown.

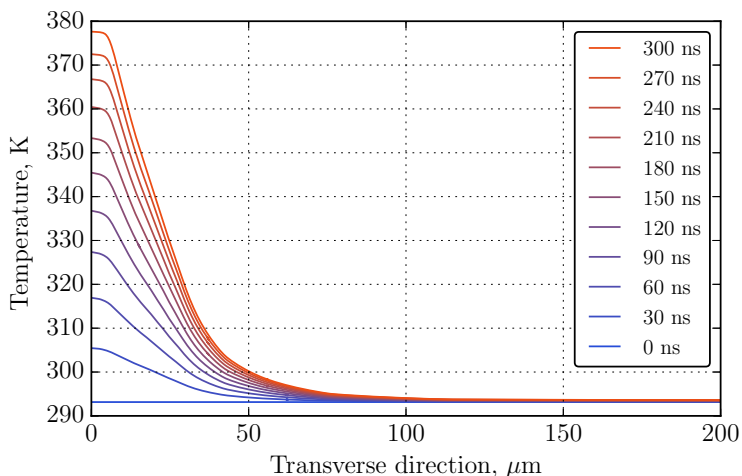


Figure 2.14: The simulation of the temperature rise in the middle of the active region of a gain guided QCL from 0 to 300 ns in 30 ns steps of a 25 V electrical pulse. One transverse symmetric half is shown.

2.3 High power pulsed driver

To optimally drive the high power lasers with high currents and voltages (up to 25 A and 25 V) in short pulses (≥ 20 ns, ≈ 5 ns rise/fall), a special pulse driver has been developed based on a fast *Metal-Oxide-Semiconductor Field-Effect Transistor* (MOSFET) driven by a dedicated gate driver (Figure 2.15). The pulse amplitude was adjusted precisely with an onboard voltage regulator circuit; control of all operating parameters and the pulse sequence as well as the measurement of the instantaneous laser current and voltage was performed by an on-board MCU (micro controller unit). Its firmware has been developed in the C programming language. Communication with the pulser is performed by a serial interface; user software was developed using the Qt cross-platform framework in the C++ programming language and has been tested on all major desktop operating systems and Android. The compact size of the board allowed placing it very close to the laser, thus minimizing current path length and stray inductance, which is critical for keeping current pulse edges sharp [75]. At a maximum operating current of 25 A and a maximum pulse repetition frequency of 1 MHz the minimum pulse width of 26.6 ns (Figure 2.16) together with 2.5 ns rise and fall times (Figure 2.17) have been measured. Following requests of users of the pulser, its basic operation modes such as periodic pulsing and the externally triggered one have been complemented by the more complex ones, such as burst mode. In this mode, the pulse sequence with a fixed repetition rate is modulated with a second order waveform, making a certain number of pulses to be followed by a number of periods with pulses off (e.g. 10 pulses followed by 30 periods without them in Figure 2.18). These additional timing parameters have been made fully user controllable as well.

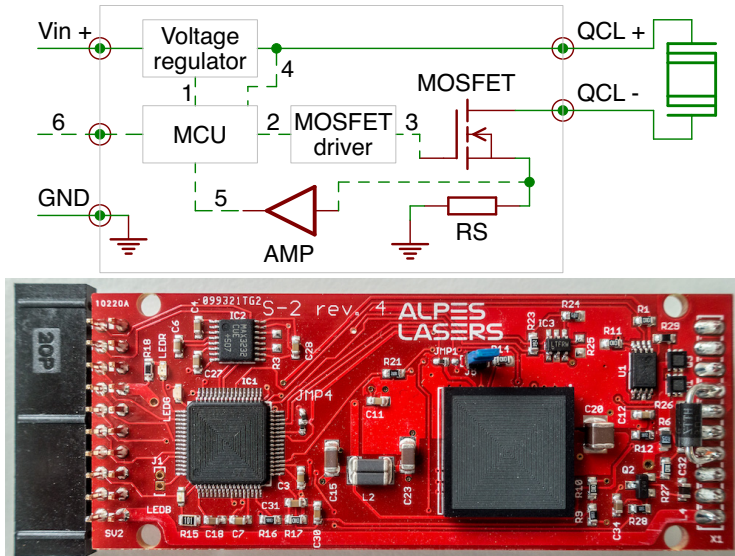


Figure 2.15: Top: pulse driver simplified schematics. V_{in} – input voltage, 1 – laser voltage control, 2 – pulse generation, 3 – amplified pulses for driving MOSFET gate, 4 – laser voltage measurement, 5 – laser current measurement, 6 – external communication and synchronization, RS – sense resistor, AMP – operational amplifier. Solid line indicates the main current path, dashed ones – supplementary signals. Bottom: board photo, size: $88 \times 33 \text{ mm}^2$.

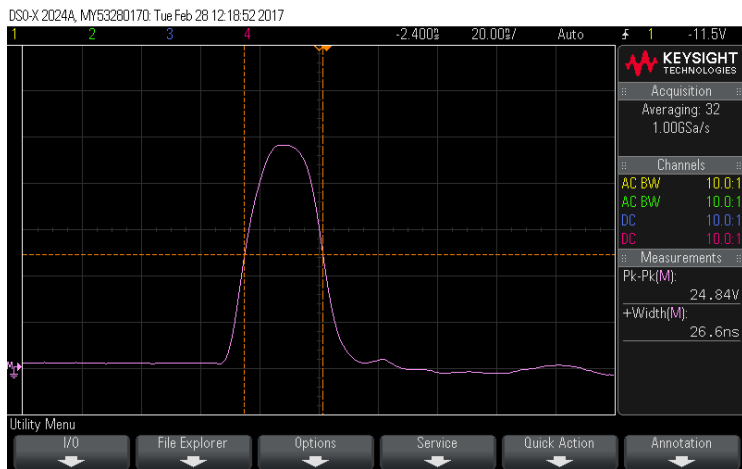


Figure 2.16: Single pulse of a minimal width: 26.6 ns and 25 A amplitude.



Figure 2.17: Measurement of rise and fall times: 2.5 ns each from 10% to 90%; amplitude is 25 A.

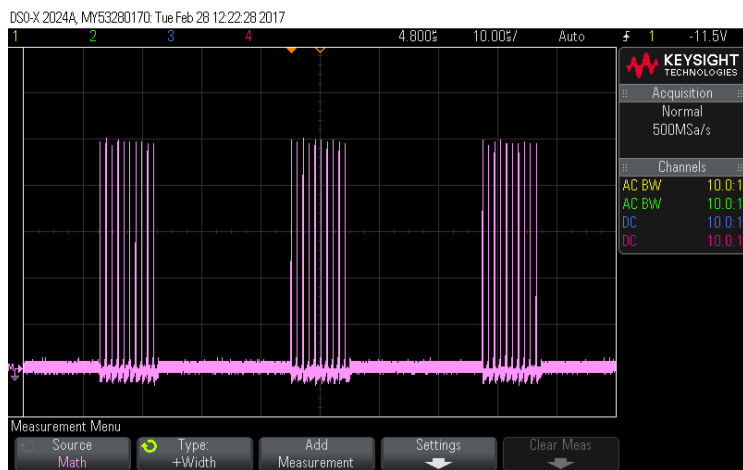


Figure 2.18: Burst mode demonstration: 100 ns pulses at the 1 MHz repetition rate, secondarily modulated with a 10x on / 30x off sequence. Amplitude: 25 A.

2.4 Conclusions

A novel configuration of the broad area pulsed QCLs has been presented along with their extensive characterization and numerical modelling. Compared to a standard design having the same active region, a larger volume of the gain medium pumped by a wide current distribution in this configuration has enabled higher peak powers, while the corresponding shape of the gain distribution provided efficient optical guiding. The lasers were driven with short high current pulses by a custom developed pulsed driver. They demonstrate a ≈ 7 times as high maximum power as ridge-waveguide devices with the same active region design. Their output beam consists of a single lobe with a ratio of $\approx 1 : 7$ between horizontal and vertical axes, which can be efficiently reshaped into a circular one with, for instance, a pair of cylindrical lenses if required. Having such properties these lasers can find their applications in remote sensing, night vision and directional infrared countermeasure systems.

3

Narrow linewidth

3.1 Linewidth and frequency noise

There is a number of ways to characterize the spectral stability of a laser – depending on the application, one or other is more convenient. First and simplest one is to measure the laser linewidth, associated with its line shape. Deeper view is given by a *Frequency Noise Power Spectral Density* (FNPSD) plot, which allows to analyze the spectral composition of the frequency noise and in many cases – determine its origins. It is typically obtained by digitally acquiring a trace of the instant optical frequency over time (an example is shown on Figure 3.1) and then employing a *Fast-Fourier-Transform* (FFT) -based conversion [76]. Simple calculations allow to convert the obtained power spectral density Figure 3.2 to the approximate line shape and linewidth [77]. For instance, the *Full Width at Half Maximum* (FWHM) linewidth is easily estimated from the value A of the area under the part with a *high modulation index* of a FNPSD plot as

$$\text{FWHM} = \sqrt{8 \ln 2 \times A}$$

In its turn, the high-modulation-index area is simply defined as the parts of the FNPSD plot above the so called β -separation line, given

by the expression [77]

$$S_{\delta\nu}(f) = 8 \ln 2 \times f/\pi^2$$

where $S_{\delta\nu}$ is FNPSD and f is the frequency. As explained in [77], any signal in the high-modulation-index area broadens the laser linewidth – while any signal outside of it contributes only to wings of the spectrum and can be neglected for estimation. Otherwise, the mentioned above digitized time trace of the optical frequency can be converted to an approximate optical line shape by plotting it as a histogram (Figure 3.3).

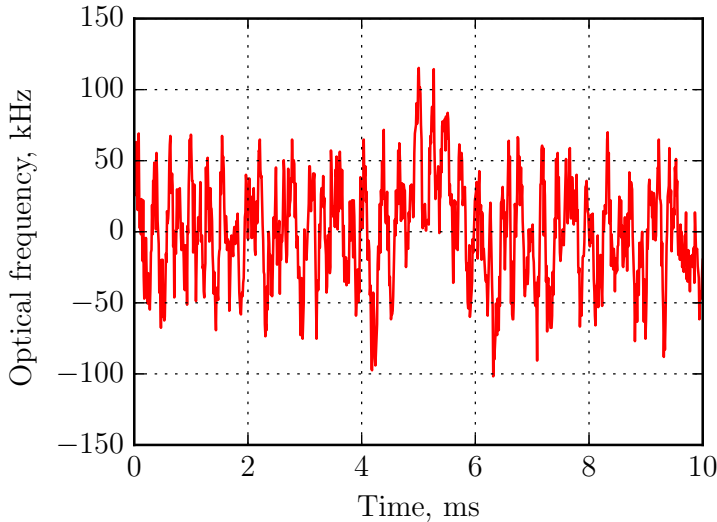


Figure 3.1: Time domain trace of the instantaneous optical frequency of a partially stabilized single mode QCL.

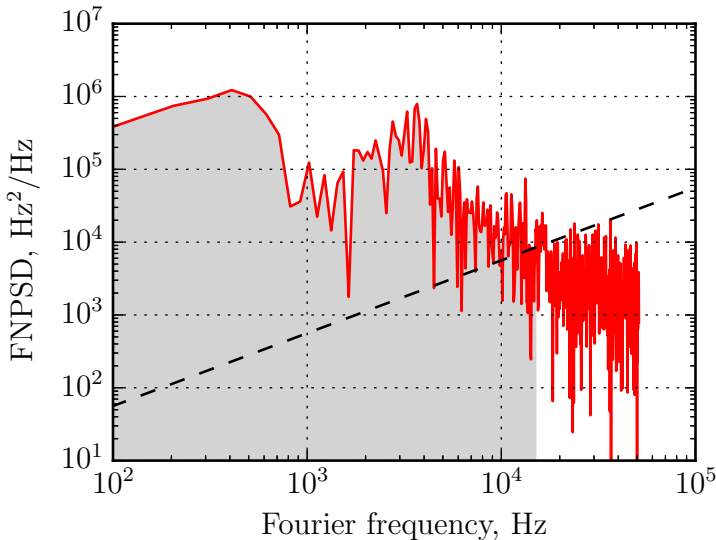


Figure 3.2: FNPSD plot (red) calculated from the trace in Figure 3.1. The dashed black line is the β -separation line. Grey is the high-modulation-index area: $1.55 \times 10^9 \text{ Hz}^2$, corresponding to a linewidth of 93 kHz (at 10 ms observation time, as follows from integration starting at 100 Hz). Note: strictly speaking, every part of the red plot above the β -separation line should be included into the integration area, and every part below should be excluded. However, as the method is intended only for the estimation of linewidth, a small simplification of the area does not change the result principally. For further examples of this approach on more complex shapes of spectra see [78].

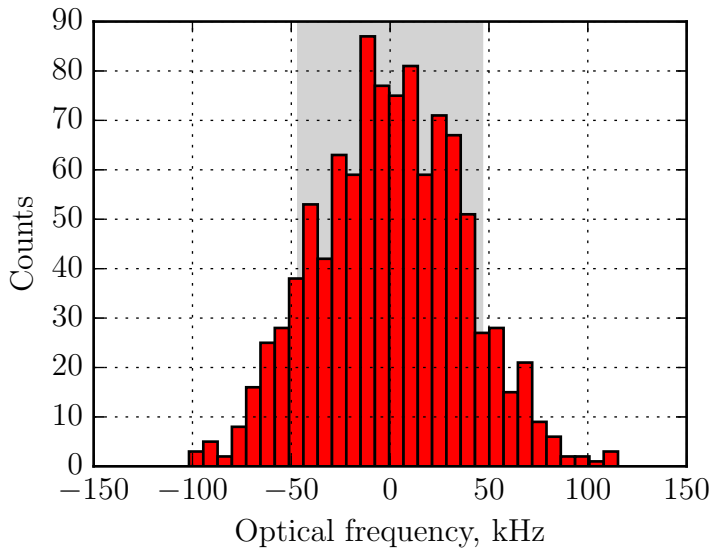


Figure 3.3: Histogram of frequency fluctuations calculated from the data in Figure 3.1. The FWHM of the histogram matches well the highlighted in gray FWHM linewidth calculated in Figure 3.1 using the β -separation line approach, indicating that the two estimation methods are well comparable.

3.2 Measuring the optical frequency

Measuring the optical frequency implies comparing it to a known reference. A few of the most common methods are highlighted here.

- Absolutely calibrated *Fourier Transform Infrared Spectroscopy* (FTIR) spectrometers and wavelength meters provide a relatively slow (seconds to minutes per measurement) way to characterize a laser spectrum with a resolution down to fractional parts of cm^{-1} . While useful for the general characterization of a laser, this resolution is a few order of magnitudes coarser than required to measure a typical single-mode linewidth of a QCL.
- Heterodyning means comparing with another known source of light – which is, ideally, spectrally narrower, than the measured one. QCL linewidths and frequency noise was evaluated carefully this way by use of stable lasers [20] and frequency combs [79]. As a variant, two identical lasers can be used to estimate their linewidth (assumed equal for both of them) [80]. Self-mixing (i.e. using the laser itself as a detector for its own light back reflected from a moving mirror) can be used as well for linewidth estimation [81].
- The third important way is based on optical elements having strong features in their transmission characteristic commonly called *frequency discriminators*. When the center frequency of the laser emission is tuned onto the steep slope of the transmission curve of such an element, the output light intensity becomes modulated with the frequency fluctuations of the laser. Combined with a sufficiently fast and sensitive optical detector, this makes a setup for measuring or suppressing the frequency noise. In the case of QCLs, convenient and widely used [25, 82–86] optical discriminators are optical cavities and gas cells. For both of them it is reasonable to choose the width of the transmission or absorption line is reasonable to choose several times wider than the linewidth of the laser which is to be measured in order to

have maximum precision of frequency noise discrimination. In case of an optical resonator, the linewidth is determined by its finesse, requiring high enough mirror reflectivity ($>99\%$) in order to achieve sufficient discriminator slope. For gases, widths of absorption lines are determined by their pressure. For instance, Figure 3.4 shows numerous absorption lines of N₂O filled into a 10 cm long gas cell at 2 mbar pressure. An important resource for investigation of absorption spectra for a given application is the HITRAN database [87], with a powerful and open access online interface available at [88].

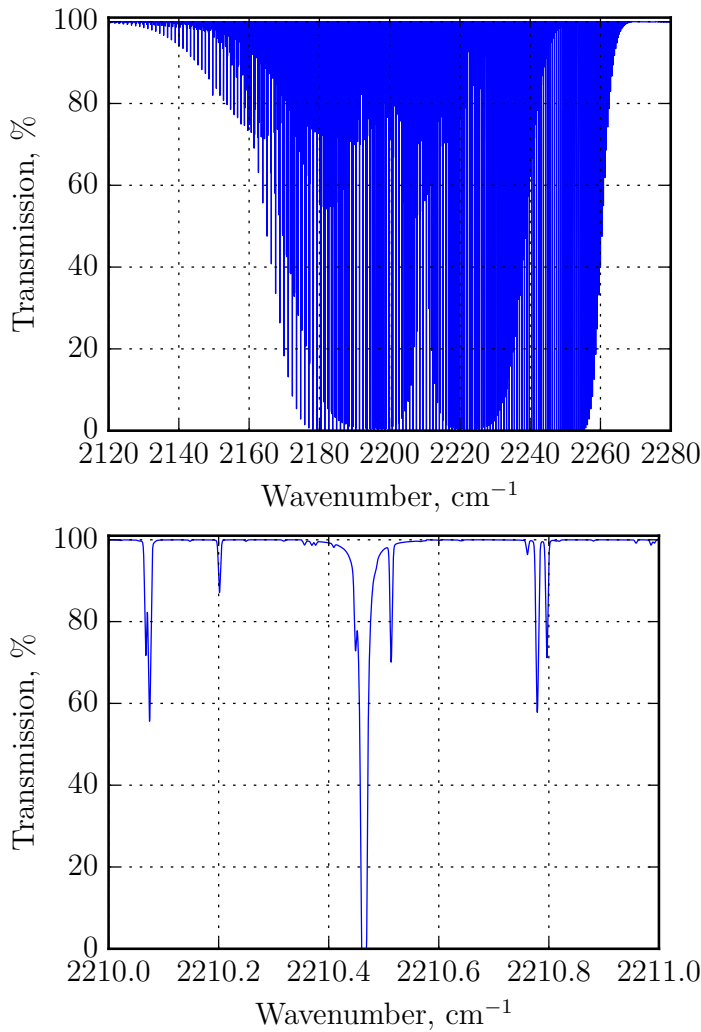


Figure 3.4: Top: absorption lines of N_2O at 2 mbar pressure with 10 cm of optical path. Bottom: zoom-in of 1 cm^{-1} in the middle of the spectrum on top, showing its fine structure.

3.3 Stabilization and noise reduction

Applications requiring frequency precision mid-infrared light have pushed the development of stabilization methods for QCLs during last years. The linewidth of a free-running distributed feedback (DFB) quantum cascade laser is typically in the range of 1 to 10 MHz [82, 84] – however, the intrinsic one is shown to be on the order of hundreds of Hz [84].

Probably the easiest way to narrow QCL linewidth down to the kHz range (from the MHz range of a free running one) is to implement a *Proportional-Integral* (PI) feedback loop on the laser current in a setup with a frequency discriminator using the optical detector output as an error signal [83]. A more complicated modulation-based method (*Pound-Drever-Hall* (PDH) , [89, 90]) in principally the same optical setup leads to even better stabilization results [91]. Many other recent studies have reported locking a QCL to an optical comb or other stable optical references [20, 92, 93], including the impressive near-1 Hz level results for configurations allowing precise tuning of the locked frequency position as well demonstrated in [94] and [95]. In the first of these works, a 5.4 μm QCL was referenced to an *Ultra-Low Expansion* (ULE) cavity by sum-frequency generation with another stable near-infrared reference. In the second one, a 10.3 μm QCL has been locked to a near-infrared optical frequency comb by generating a sum frequency with one comb tooth at 1.82 μm and comparing this sum frequency to another comb tooth at 1.55 μm . Ultimate narrow-linewidth performance at the sub-10-Hz level has been recently reported for a QCL phase-locked to a secondary frequency standard made of a CO₂ laser stabilized onto a saturated absorption line of OsO₄ [96]. Another interesting solution is based on optical injection: a small amount of light generated by a frequency stable radiation source, such as a difference-frequency comb-referenced one, can force a QCL to inherit the frequency stability, while providing the hundreds of times amplification of the output power [86].

For some applications, like high-resolution spectroscopy, there is a

challenge of narrowing the linewidth while preserving the maximum tuning range of the laser. For this reason, the development of linewidth narrowing techniques that do not involve a fixed optical frequency reference and which can be implemented in a cost-effective integrated configuration is quite attractive.

3.4 Frequency noise in QCLs

The minimal linewidth of a laser is fundamentally limited by the spontaneous emission. The first formula for the limit was derived by Schawlow and Townes [97]; then Henry has improved it for semiconductor lasers [98] by accounting for the coupling between changes of gain and refractive index, i.e. including the LEF, resulting in:

$$\Delta\nu = \frac{1}{4\pi} \frac{\hbar\nu}{P} \alpha_m \alpha_{tot} v_g^2 n_{sp} (1 + \alpha_{LEF}^2)$$

where $\Delta\nu$ is the laser linewidth, ν is the lasing frequency, P is the output power, α_m and α_{tot} are the out-coupling losses and the total losses, v_g is the group velocity, n_{sp} is the rate of spontaneous emission, and α_{LEF} is the LEF. The value of latter is in the range of 2-6 for diode lasers [99–101], leading to an order of magnitude increase of $\Delta\nu$. On the contrary, α_{LEF} is close to zero for DFB-QCLs, which are typically designed to lase at the peak of their symmetric gain curve [40, 41] – thus not affecting the linewidth limit. In addition, relatively low mirror losses, higher output powers and lower optical frequencies provide QCLs with better results in this comparison. The typical value is in the range of hundreds of Hz [84, 102].

However, in a free running QCL, even powered with a sufficiently low noise current source, i.e., one, for which contribution to the linewidth through the electrical modulation is negligible (with a current noise spectral density under $1nA/\sqrt{Hz}$) [103], an intrinsic linewidth of few hundred Hz is never observed. Instead, it is over thousand times broader, reaching MHz levels. Observations of voltage fluctuations on laser contacts [104] and their high correlation ($\approx 90\%$) to optical frequency fluctuations [82] allow to assume, that, as in other types of semiconductor devices [105–109], this kind of noise is generated by the laser structure itself – and leads to linewidth broadening.

The studies of FNPSD of free-running single-mode QCLs reveal 1/f trend in its dependency on frequency. Further detailed investigations of dependency of noise magnitude on temperature (it is higher at low temperatures [104]), device internal geometry (ridge waveguide lasers

demonstrate lower noise compared to their buried heterostructure-type analogs [110, 111]) and doping profile (careful placement of doping inside the active region can lead to lower electronic noise figures [9]) allow to assume, that the noise is generated by the processes in the internal semiconductor structure (such as leakage currents [112], electron trapping and detrapping on impurity states [113] and lattice scattering [114]) and influences the laser instant frequency through the dissipated electrical power.

A QCL can be represented as an active region with a differential electrical resistance R_{diff} (which is assumed to be constant within a small current range) and a serially-connected noise resistance δR . The active region then dissipates a constant electrical power when the laser is operated in the standard constant-current mode, and the overall electrical power fluctuations are induced by the instantaneous variations δR of the noise resistance. This leads to fast changes of the QCL internal temperature resulting in a modulation of the optical frequency as this latter directly varies with temperature at a typical tuning rate of

$$\frac{1}{\nu} \frac{d\nu}{dT} \approx 10^{-4} \text{K}^{-1}$$

where ν , $d\nu$ and dT are frequency, its variation and the variation of temperature [115]. It should be noted, that the mechanism of electrical wavelength modulation of QCLs is purely thermal – again, due to the value of LEF, different from the interband semiconductor lasers, where wavelength can be modulated quickly via carrier density [116, 117].

Based on the relative easiness of measuring the voltage fluctuations generated by a QCL, some interesting methods of noise stabilization can be developed. Indeed, if one manages to compensate quickly enough the induced temperature fluctuations, the optical frequency can be made significantly more stable without making any direct measurement of it. One method was demonstrated in [82] employing external illumination of the QCL under test with another laser, the intensity of which was proportional to the QCL voltage noise.

Another way proposed in the same work would make use of micro-heaters embedded into the QCL waveguide close to the active region [12] which would lead to tighter integration of the stabilization loop. Both methods face the same limitation: the time it takes for a heat wave generated on top of the laser to reach the active region is on the order of ten microseconds [12, 118], thus limiting the useful modulation bandwidth to about 100 kHz. A significantly higher bandwidth of frequency modulation is reachable with electrical current modulation [80, 118]. However, this way of frequency control is less straightforward to combine with simultaneous measurement of voltage fluctuations, as current modulation itself induces a change into the measured voltage signal. In this situation, a more advanced scheme of signal processing is required.

3.5 Constant power laser driver: digital implementation

3.5.1 The design idea

A novel method of QCL frequency noise reduction is presented here. It exploits the voltage noise measured at the laser contacts, but uses fast digital signal processing to directly stabilize the electrical power dissipated in the QCL by feedback to the laser injection current.

If one aims at reducing the frequency noise of a QCL using the measured voltage as an error signal for a proportional-integral (PI) servo-loop, the obtained correction signal cannot be directly applied to the laser injection current as it does not lead to any stabilization of the electrical power dissipated in the QCL. The reason is that, while the laser voltage noise is effectively reduced in this way (corresponding to an operation in constant voltage supply mode, see Figure 3.7), injection current modulation is induced at the same time, leading to a dissipated-power modulation of the same magnitude as in the non-stabilized case. Such a feedback loop only converts voltage noise into current noise, but the associated temperature and optical frequency fluctuations are basically unchanged. As neither a stable voltage nor a stable current alone leads to low frequency noise operation of a QCL, it is important to produce a proper error signal that is directly proportional to the electrical power fluctuations, i.e., to the product of the QCL voltage and current.

Ideally, one would do a direct multiplication of full values of current (I) and voltage (V) applied to the laser and then use the product (full power, $P=I \times V$) as an error signal for a feedback loop to make it constant. Power supplies based on such a principle do exist [119]. However, when applying this to a QCL, problem arises with the dynamic range of the measured signals. Fluctuations of the laser voltage have magnitude of microvolts, and this has to be observed on top of ≈ 10 V of DC voltage. Such a dynamic range (10^7) is barely reachable with best modern digital or analog circuits. This can be overcome by AC coupling the signals before amplifying them, thus removing the large DC offset.

For the noise resistance model described above, the instantaneous power variations can be written as

$$\delta P(t) = I_0 \delta U(t)$$

when the laser is driven by a constant current I_0 , where $\delta U(t)$ is the measured voltage fluctuation induced by the noise resistance. Under the applied current corrections $dI(t)$, which are small compared to the average current I_0 , the instantaneous power variations become in first order approximation

$$\delta P(t) = U_0 dI(t) + I_0 \delta U(t)$$

where U_0 is the average voltage drop across the laser corresponding to I_0 . Therefore, four parameters are needed to calculate the error signal $\delta P(t)$: the average voltage U_0 and current I_0 , and their instantaneous variations δU and dI , respectively. From this error signal, a control of the laser current can be applied via a PI servo-controller to stabilize the electrical power applied to the laser and thus reduce the optical frequency fluctuations. It is important to emphasize that this way of controlling the laser current does not impose any restrictions on laser operation temperature and current and therefore preserves full range of the optical frequency tuning.

The signal processing described here was implemented in a commercially available *Field-Programmable Gate Array* (FPGA) evaluation board with fast 14-bit *Analog to Digital Converter* (ADC) and 14-bit *Digital to Analog Converter* (DAC) . The ADC and DAC were operating at 20 MHz and the overall reaction time of the output signal to a change of the input signal was 7 ns. The average values of the QCL voltage and current were not measured by the FPGA board, but were accounted for in the processing algorithm as user-changeable parameters, as they remained constant during the stabilization experiment. This is justified as the stabilization method presented here corrects for fast frequency fluctuations of the QCL to reduce its linewidth, but does not compensate for the long-term wavelength drift of the laser.

The small variation dI of the laser current caused by the stabilization was also not measured, but taken from the output value of the stabilization algorithm corresponding to the previous time step. This simplification is valid as long as the variation of current in the laser exactly follows the output of the stabilization circuit. Such an assumption can indeed be done for the described setup, as, first, the used constant current source is very low noise, and, second, its modulation input is well linear. Therefore, only one parameter was measured in real-time by the FPGA-board, i.e., the laser voltage fluctuations δU , and one ADC was sufficient to produce the error signal.

3.5.2 Experimental setup

A scheme of the implemented experimental setup is displayed in Figure 3.5.

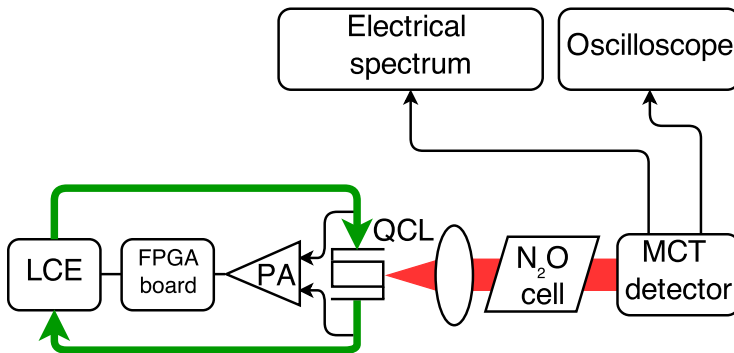


Figure 3.5: Scheme of the experimental setup. LCE – laser control electronics (current driver and temperature controller), PA – preamplifier, bold arrows represent electrical current through the QCL.

The QCL under test was driven by a low-noise current source developed at Laboratoire Temps-Fréquence, with a typical current noise density lower than $1 \text{ nA}/\sqrt{\text{Hz}}$ at all frequencies above 1 kHz. This

noise level is sufficiently small to insure that it does not induce any additional linewidth broadening of the QCL [103]. The voltage noise measured at the QCL contacts was amplified using an AC-coupled low noise preamplifier (Signal Recovery model 5113) with a gain of 34 dB, a low cut-off frequency of about 1 Hz and a high cut-off frequency of 300kHz (which was in this experiment the limitation for the overall loop bandwidth), and was continuously processed by the FPGA board. The fluctuations of the electrical power dissipated in the QCL were calculated from the measured amplified voltage fluctuations combined with the other parameters stored in the FPGA. The output signal of the board, i.e., the calculated drive current correction dI necessary to minimize the dissipated power fluctuations, was fed as an input voltage into the modulation port of the laser current source. To characterize the spectral properties of the stabilized laser, its emission wavelength was tuned to the flank of an N₂O gas absorption line obtained from a 10-cm long sealed gas cell filled at 2 mbar pressure and acting as a frequency discriminator. A fast thermo-electrically cooled *Mercury Cadmium Telluride* (MCT) detector (Vigo PVI-4TE-08) measured the optical power transmitted through the gas cell, in which the laser frequency noise has been converted into amplitude noise by the linear slope of the N₂O transition. The output signal of the amplified photodiode was analyzed with a fast Fourier transform (FFT) spectrum analyzer (Stanford Research System SR770) to measure the laser frequency noise power spectral density (PSD). For the demonstration of this new frequency noise reduction technique, two 7.9- μm DFB buried-heterostructure QCLs produced by Alpes Lasers have been compared, and demonstrated very similar results. Therefore, experimental results are shown here for only one of them. The laser was operated at 15 °C and was precisely temperature-stabilized at the mK level using a temperature controller that is part of the low-noise QCL control electronics. The laser was operated at a constant current of 0.7 A and a corresponding voltage drop of 12 V, with an output optical power of 20 mW.

3.5.3 Calibration

The calibration of the N₂O absorption line used as a frequency discriminator was obtained by spectroscopic measurements. First, a laser current scan performed from 690 mA to 740 mA at a constant temperature of 15 °C was used to reveal two N₂O absorption lines at 1272.85352 cm⁻¹ and 1272.29068 cm⁻¹ [87]. The center frequencies of these transitions were used to determine the laser current-tuning rate of 434.7 MHz/mA (another way used during this work to measure frequency tuning is shown in Appendix B). Then a narrower scan of a single absorption line was realized with 0.01 mA current steps to precisely determine the slope of the linear range on the side of the absorption line. The measured discriminator slope $D = 0.921$ V/MHz was used to convert the noise spectra measured at the output of the photodiode and recorded by the FFT spectrum analyzer into laser frequency noise.

3.5.4 Results

Figure 3.6 illustrates the effect of the all-electrical frequency-noise-reduction method applied to our QCL by comparing the frequency noise PSD measured on the side of the N₂O absorption line for the free-running and stabilized QCL. A uniform reduction of the frequency noise PSD by one order of magnitude is achieved up to a frequency of 100 kHz, which was the upper limit of our FFT spectrum analyzer. The QCL frequency noise reduction factor achieved here is comparable to the one previously obtained when controlling the QCL internal temperature using an external near-infrared laser [82]. However, the new method proposed here is simpler to implement as it does not require any additional optical component out of the QCL. The corresponding full width at half maximum (FWHM) of the QCL emission line calculated using the β -separation-line approximation described in [77] is reduced from 1730 kHz for the free-running laser down to 480 kHz for the stabilized laser (at 10 ms observation

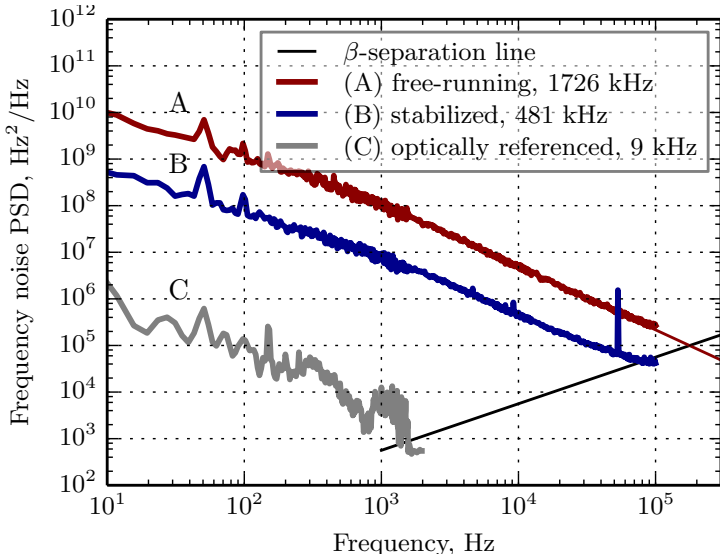


Figure 3.6: Frequency noise PSD of the QCL measured under free-running (A) and stabilized (B) conditions. The thin line above 100 kHz for the free-running QCL is an extrapolation of the $1/f$ noise used for the linewidth determination. The 'C' curve shows the frequency noise reduction achieved when stabilizing the QCL frequency to the side of the N_2O transition using the same stabilization electronics and the optical signal from the MCT detector as an error signal. The corresponding full width at half-maximum (FWHM) linewidth of the laser calculated using the concept of the β -separation line [77] is also indicated in each case (at 10-ms observation time).

time). For the free-running QCL, the noise at frequencies higher than 100 kHz still contributes to the laser linewidth and the crossing-point of the noise spectrum with the β -separation line (which corresponds to the upper integration limit for the linewidth determination) was estimated to be 177 kHz by extrapolating the $1/f$ noise to higher frequencies (thin line in Figure 3.6). Figure 3.6 also presents the QCL frequency noise obtained using the same stabilization electronics, but in the case of an optical stabilization to the side of the N_2O absorption

line, using the signal of the MCT detector instead of the computed electrical power as an error signal. Though this measurement was obtained in-loop, i.e. by the same detector, which signal is used for the feedback, it is an order of magnitude higher than the noise floor determined by intensity noise of the laser. Its purpose is the indication, that the effectiveness of the noise reduction achieved with the stabilization of the electrical power is limited by the partial voltage-to-frequency noise correlation and not by the stabilization electronics. In addition to the frequency noise, the intensity noise spectrum of the QCL was measured in free-running and stabilized operation modes. The measurement was made using the same setup as shown in Figure 3.5, but without the gas cell. No measurable change of the laser intensity noise was observed.

Figure 3.7 presents the laser voltage noise PSD measured for the QCL operated in free-running mode (curve 'D') and with the electrical power stabilization activated (curve 'E'). Only a tiny reduction of the voltage noise is observed when the stabilization is activated, which is much smaller than the reduction of the frequency noise shown in Figure 3.6. In addition, the lower voltage noise achieved when using the QCL voltage fluctuations as the error signal for the PI-loop instead of the calculated electrical power is also displayed in Figure 3.7. Despite the higher decrease of the voltage noise, no optical frequency noise reduction is achieved in this case as explained before.

The fluctuations of the QCL voltage and optical frequency were simultaneously recorded by a digital oscilloscope over a timescale of 20 ms when the stabilization was activated as shown in Figure 3.8. The corresponding fluctuations of the QCL electrical power (as calculated by the FPGA) are also displayed in the figure. The effectiveness of the loop to reduce the fluctuations of the electrical power dissipated in the QCL is clearly seen when the loop is activated ($t > 10$ ms), which results in a corresponding decrease of the optical frequency fluctuations. It is interesting to notice that in this case, neither the QCL voltage, nor the current, is stable (as the current constitutes the feedback sig-

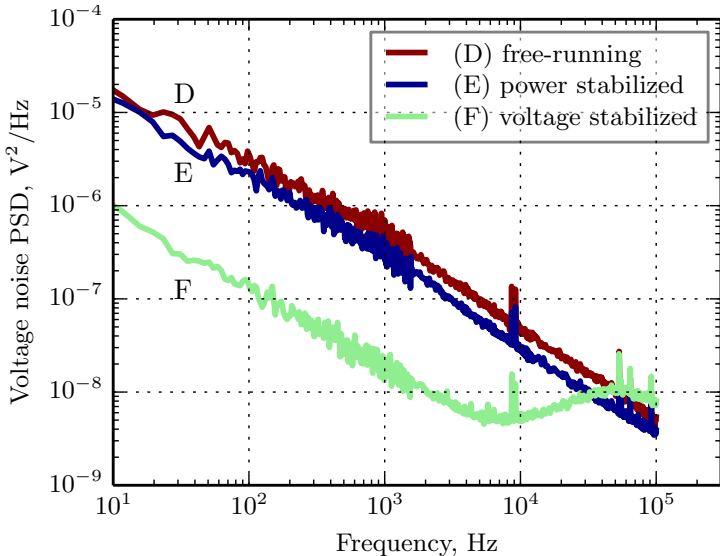


Figure 3.7: Voltage noise power spectral density compared for the free-running and stabilized QCL. The 'E' curve corresponds to the main result of this work with laser electrical power stabilized. The 'F' curve shows the limit to which voltage noise can be PI-suppressed.

nal), but only the electrical power is stabilized. From the recorded time series, the correlation coefficient between the fluctuations of the optical frequency and QCL voltage has been calculated, leading to a value of 0.75 for the free-running laser and 0.02 for the stabilized laser. This indicates that the contribution to the laser frequency noise originating from electrical power fluctuations is efficiently reduced.

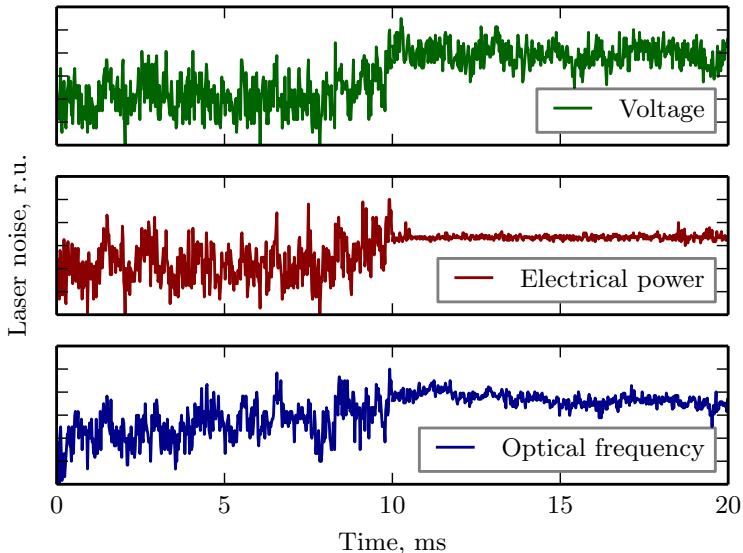


Figure 3.8: Simultaneous time series of the measured voltage, calculated electrical power and measured optical frequency fluctuations for the free-running ($t < 10$ ms) and stabilized ($t > 10$ ms) QCL.

3.6 Constant power laser driver: analog implementation

3.6.1 Motivation

The setup described above has served well for the first demonstration of the principle of electrical power stabilization. However, in order to push the technology closer to real world applications and possibly achieve even better performance, a next step was made. It was decided to integrate electronic pieces of the setup (low noise current source, voltage amplifiers, signal processing) on a single board – like this a single compact device could be made better immune to external noise sources, and also reach higher stabilization bandwidth due to physically shorter connections. Simultaneously, digital processing (scaling and addition of voltage and current fluctuations) was replaced with analog one. Although being less straightforward to implement,

this can have advantages of higher dynamic range (still limited in digital case by resolution of AD/DA converters even in case of AC coupling of input signals) and potentially lower noise floors. The new design was started from an electrical *Simulation Program with Integrated Circuit Emphasis* (SPICE) model of a circuit (using the freely available LTSpice software), growing from its basic parts to a complete system. Therefore, it is described along with results from simulations of successive circuit parts. The overall circuit block diagram is given on Figure 3.9.

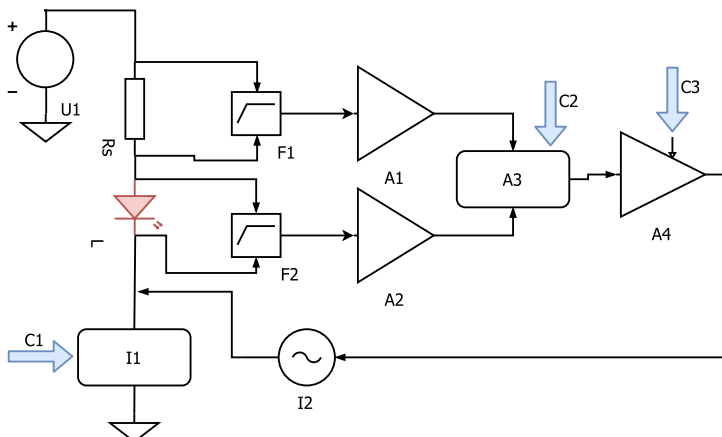


Figure 3.9: Principal diagram of an analog power stabilized power supply. U1 is a constant voltage source; Rs is a current sense resistor; L is the load (a QCL); I1 is the constant current setting circuit – these elements form a usual Libbrecht-Hall style low noise current sink. Further added elements for the power stabilization loop are: F1 and F2 – band-pass filters; A1 and A2 – instrumental amplifiers; A3 – summing amplifier; A4 – loop gain control amplifier; I2 – voltage controlled AC current correction circuit closing the loop. C1 is constant current control input; C2 is a control for balance between inputs in A3 summing circuit; C3 is a gain control input.

3.6.2 Low noise constant current source

As described in the previous section, the constant-power supply is built on top of a low-noise constant-current supply which, powering the laser at the user-chosen level of current, allows to observe its voltage fluctuations, and has a modulation input in order to compensate for them. Most common implementations of a low noise constant current source (or sink, depending on the desired polarity) for lasers are based on the Libbrecht-Hall design [120]. It was originally proposed for diode lasers, typically requiring lower currents and compliance voltages, then QCLs, and then updated a number of times [121–123] by adding digital controls, higher operation ranges, safety features and even further improving noise performance. Particularities of applying such a design to QCLs and fundamental limits of its operation can be found in a thorough review by M. Taubman [124].

3.6.3 Design and simulations

A simple model of a noisy QCL, consisting of a serially connected $5\ \Omega$ resistor ($rR1$) and noisy 9 V voltage source ($rB1$), was put into minimal low noise constant current sink configuration similar to the one in Libbrecht-Hall design (Figure 3.10). This way the simulation was supported by the realistic magnitude of power fluctuations in a QCL driven with a stable current source and as a reference point for further improvement (however, more complicated and precise SPICE models of QCLs exist [125, 126] e.g. for simulating their dynamic responses). Further components of the circuit include: $rQ1$ – a power MOSFET setting the current in the laser; $rU1$ – a low noise operational amplifier comparing the actual current (measured on sense resistors $rR7$ and $rR9$) to the setpoint (presented here for simplicity as an ideal voltage source, $rVref$); $rR5$, $rR6$, $rC6$ – components of snubber filtering network as described in [120]; $rL1$ – filtering inductor; $rV+laser$ – a low noise external voltage regulator, powering the circuit; $rR3$ – series resistor, used for current measurement in further

steps of design; rC4/rC5 – power supply decoupling capacitors. Not shown in the circuit are the +P and -P voltage supply rails for the operational amplifier. As configured, the circuit supplies 400 mA into the device under test (2 V at rV_{ref} / 5Ω ($rR7+rR9$ in parallel) = 400 mA) (Figure 3.11).

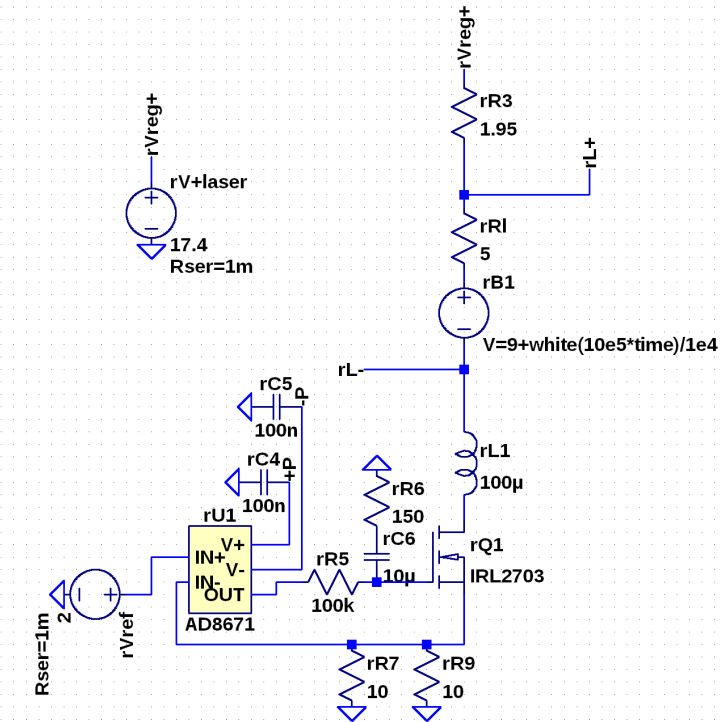


Figure 3.10: Schematic of a low noise Libbrecht-Hall current sink connected to a noisy QCL load.

This circuit has been left intact as a reference; another side-by-side copy of it was complemented by components for a power-stabilized driver model. Band pass RC filters were added to decouple voltage and current fluctuations which have to be measured from their high

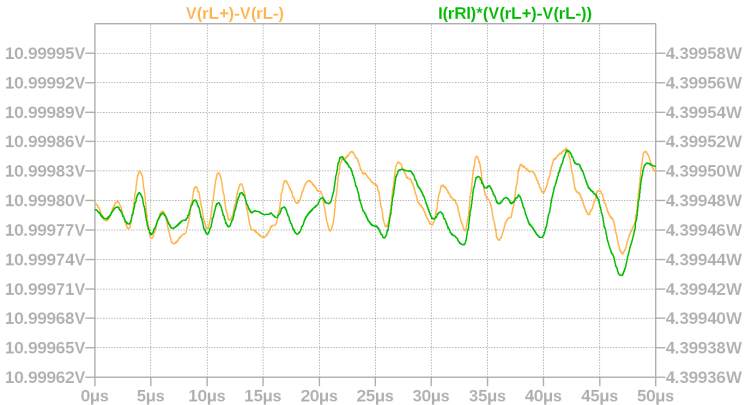


Figure 3.11: Modeled voltage and power noise of a free-running QCL.

DC offset levels to reduce the requirements for the dynamic range of the circuit (Figure 3.12). Low pass time constants for such filters should be as low as possible (as the targeted flicker noise $1/f$ spectrum is not limited at low frequencies). On the other hand, in order to keep the noise floor of the input stage low compared to the small measured signals, resistor values have not to exceed the $k\Omega$ range due to Johnson-Nyquist noise:

$$v_n^2 = 4k_B T R$$

where v_n is the amplitude spectral density of the voltage noise, k_B is the Boltzmann constant, T is the absolute temperature, and R is the value of the resistor. This gives an estimate of $4 \text{ nV}/\sqrt{\text{Hz}}$ for a $1 \text{ k}\Omega$ resistor at room temperature. Also, lower resistor values are better to keep the input offsets of the following amplification stage low. The capacitor values of the filter are practically limited by compliance voltage requirements (25 V at least to safely cover most of QCLs) and physical dimensions. In order to introduce minimal distortion into the frequency response, film type capacitors were chosen [127]. Final combinations of $1 \text{ k}\Omega$ resistors and $10 \mu\text{F}$ capacitors gave a

reasonably low -3 dB cutoff frequency of 15 Hz. The high frequency response was limited intentionally at 2 MHz in order to eliminate gain in the whole feedback loop at frequencies where the total phase delay exceeds 180 degrees. The simulated response of the input filter is shown on Figure 3.13.

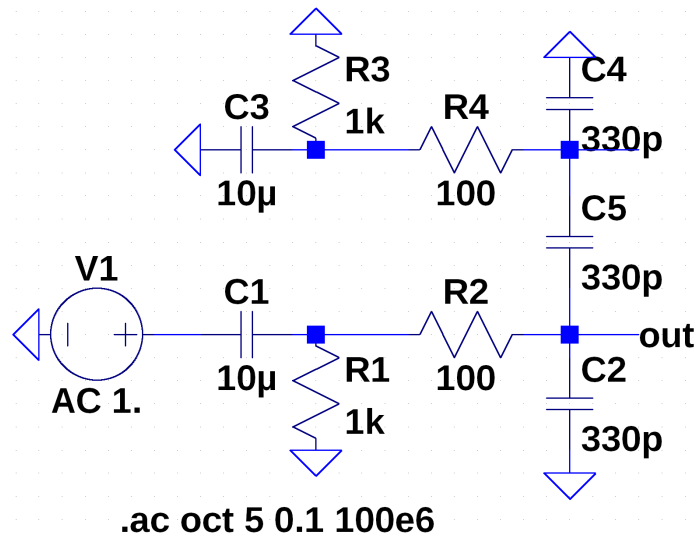


Figure 3.12: Bandpass input filter electrical model, connected to a test signal generator (shown as V1).

After this, a signal amplification stage was added (Figure 3.14). Two equal low-noise and high-gain instrumentation amplifiers in identical configurations were used for current and voltage measurement branches in order to have exactly the same frequency response for both amplified values and therefore introduce minimal distortion into the measured power. An Analog Devices model AD8429 [128] was chosen for its very low ($1 \text{ nV}/\sqrt{\text{Hz}}$) input referred noise level and sufficient bandwidth (1.2 MHz at gain = 100).

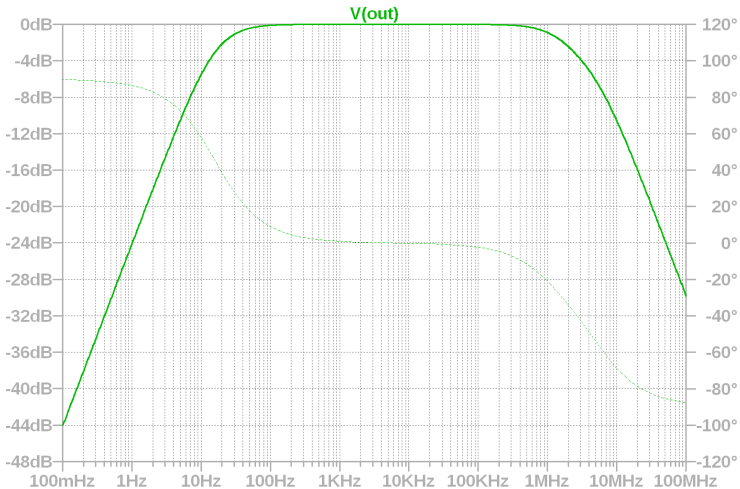


Figure 3.13: Simulated magnitude (solid line) and phase (dotted line) responses of the bandpass input filter.

The next step in the signal processing chain is to sum the amplified voltage and current fluctuations in order to obtain the power fluctuation: $\delta P = I\delta U + U\delta I$. For a fixed point of laser operation (constant I and U), this could be done with a simple voltage adder made of two resistors. However, as one of the design goals was to develop a user-friendly instrument, resistors had to be replaced with some easily externally controllable circuit. Amongst multiple existing solutions of this problem (digital potentiometers, voltage controlled amplifiers, dedicated analog multipliers, DACs with fast reference voltage inputs) no solution was found matching low noise, high bandwidth and sufficient precision requirements. Finally, the desired circuit was found in a book [129] together with a story of its design process. The LT1251 chip [130] was designed for video fading applications, but, being a dual high bandwidth voltage controlled amplifier with summing output, fitted perfectly the needs of current design. Two of those chips were used in a row (Figure 3.15), first one adding with scaling the am-

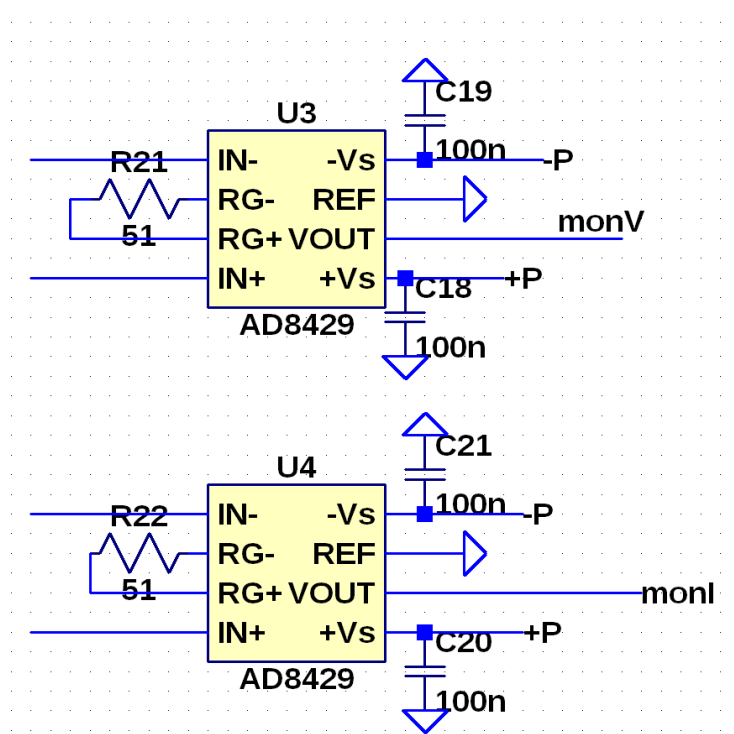


Figure 3.14: Equivalent instrumentational amplifiers sub-circuits used for amplification of current and voltage fluctuations in the load. Differential inputs on the left are connected to bandpass filters; outputs on the right (monV, monI) are summed with a further circuit. +P and -P are the power supply rails.

plified voltage and current variations in order to produce the correct error signal, and the second one amplifying or attenuating the level of this signal. In order to achieve best stabilization performance, the calculated power fluctuation has to be fed back into the laser current with negative sign (the increase of power has to be compensated with reduction of current and vice versa) and correct magnitude – so that it reduces fluctuation as much as possible, but does not cause self-oscillations of the loop. As LT1251 has sufficient current source/sink capabilities (40 mA), a resistor was simply connected from its output to the negative contact of the laser under test, implementing the signal path for current correction. The complete circuit is shown in Figure 3.16.

For the hardware implementation, the values of the components of the current sink part (current sense resistors, precise voltage reference) were selected for the maximum load current of 1 A, this way keeping a balance between current noise level, power dissipation and requirements for high-power QCLs. To save development time, the controls of the circuit (C1-C3) have been embodied with multi-turn potentiometers. However, these are straightforward to replace with slow, low noise and high resolution DACs in order to finish the design as a scientific instrument.

As shown in Figure 3.17, the final modeled circuit was able to reduce the power fluctuations in a noisy load by more than an order of magnitude as compared to the reference one operating in constant current mode.

3.6.4 Characterization

The circuit has been built on a 8 cm × 10 cm PCB (Figure 3.18) with most of the signals passing on one side of it, leaving the second one for a large ground polygon, helping with noise immunity. It has been mounted in a metallic box (Figure 3.19) together with the voltage regulator boards powering it (three small green boards) for a complete

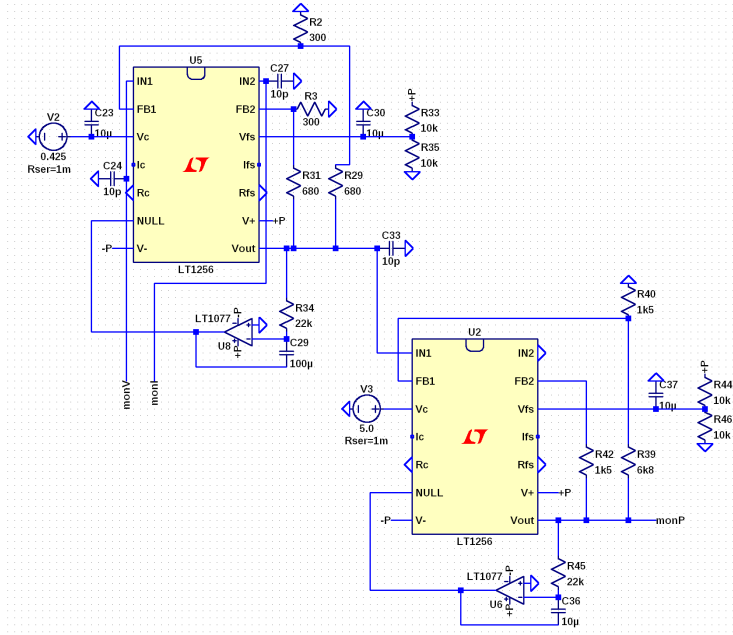


Figure 3.15: Chain of two voltage controlled amplifier circuits, the first of which (U5) generates the correct load power fluctuation value by summing its inputs (monV , monI) with scaling according to the control input value (V_2); the second one (U2) scales the output signal (monP) according to the second control input value (V_3). The offset cancellation circuits with U8 and U6 are taken from the LT1251 datasheet [130].

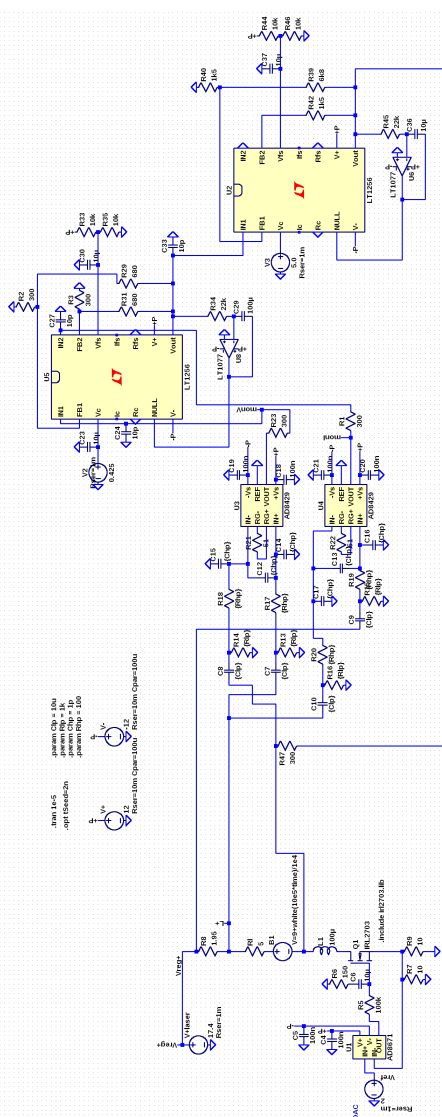


Figure 3.16: Complete circuit diagram joining together all the previously mentioned parts.

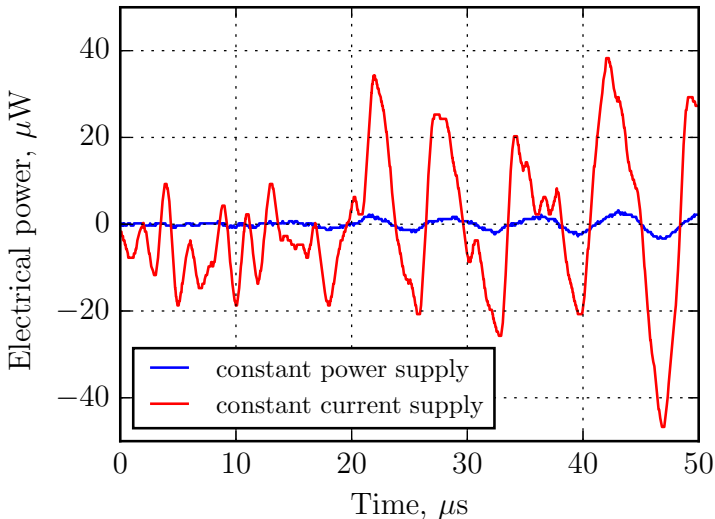


Figure 3.17: Simulated electrical power fluctuation traces in a noisy QCL model powered by a low noise constant current supply (red) and the same one complemented by a power stabilization circuit (blue). The ratio of standard deviations of the two signals exceeds 13.

shielding of electromagnetic interference.

Then, the resulting signal processing chain gain and bandwidth have been measured by connecting its input to a strongly attenuated signal generator output and comparing the square waveform on the circuit input to the one on its output (Figure 3.20). A maximum gain value of 2050 was measured together with 5 MHz -3 dB bandwidth, matching well the design values.

The performance of the constant-current part of the developed circuit has been characterized by driving a test load (32Ω resistor) at various drive currents (0.05 A to 0.8 A) and measuring voltage fluctuations on it using the power stabilization part of the circuit as a high-gain and high-bandwidth measurement amplifier. The power stabilization loop was not closed in this case, and only one amplifier branch out

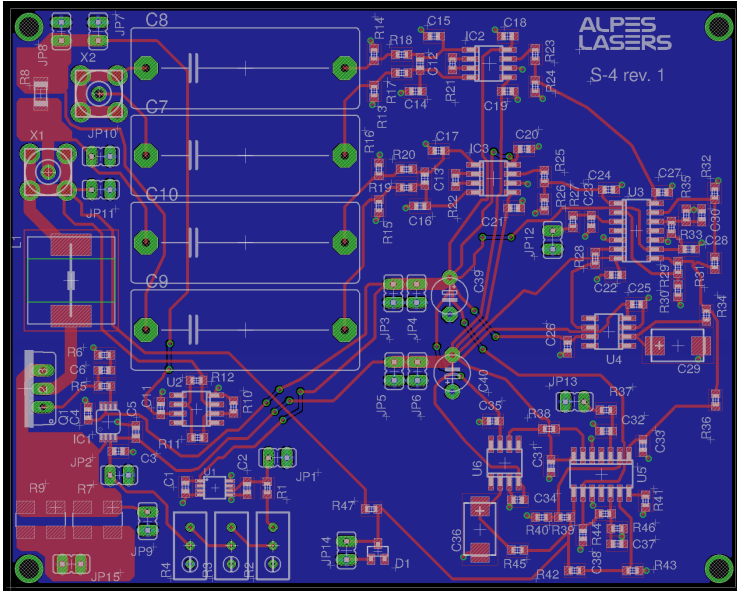


Figure 3.18: PCB layers (top in red color, bottom in blue color) of the implemented circuit.

of two (dedicated for voltage fluctuations) was used. Knowing the gain of the amplification chain and the value of the load resistor, the measured voltage noise traces have been converted to current noise ones. Then, the current spectral density was calculated using Welch's periodogram method [76]. As seen in Figure 3.21, the noise level of the developed circuit is better than the one for a commercially available low-noise QCL driver [131]. The RMS current noise in a 100 kHz bandwidth was measured at the 0.18 μA level (versus 0.4 μA for the compared one).

3.6.5 Results

The driver has been tested with a single mode 4.6 μm QCL in a setup similar to the one described in section 3.5. This time absolute calibra-

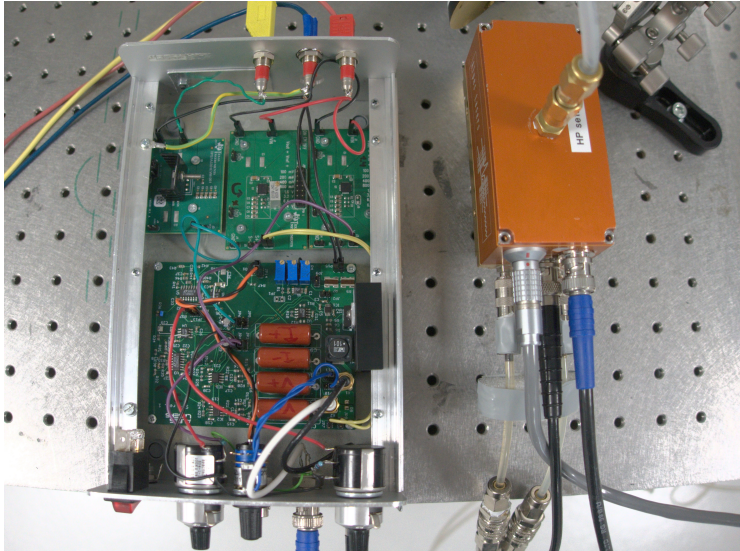


Figure 3.19: Photo of a complete power stabilized driver (on the left) powering a QCL in *Laboratory Laser Housing* (LLH) package (on the right).

tion of optical frequency discriminator slope has not been performed, as noise reduction performance can be evaluated without it.

In order to perform a precise tuning of the circuit, a supplementary live signal analysis tool has been developed based on continuously capturing and processing waveforms from a fast digital oscilloscope. Calculating the value of the correlation between traces from two input channels, it has been used to set precisely the balance control input value (C2 in Figure 3.9). In this case, one oscilloscope channel has been connected to the optical detector measuring the discriminated optical frequency noise of a laser, and the second one to the output of the circuit calculating power fluctuations. As has been observed during the simulations, the maximum achievable value of noise suppression in such a circuit depended strongly on the precise setting of this control, i.e. the U/I ratio in the $\delta P = I\delta U + U\delta I$ expression.

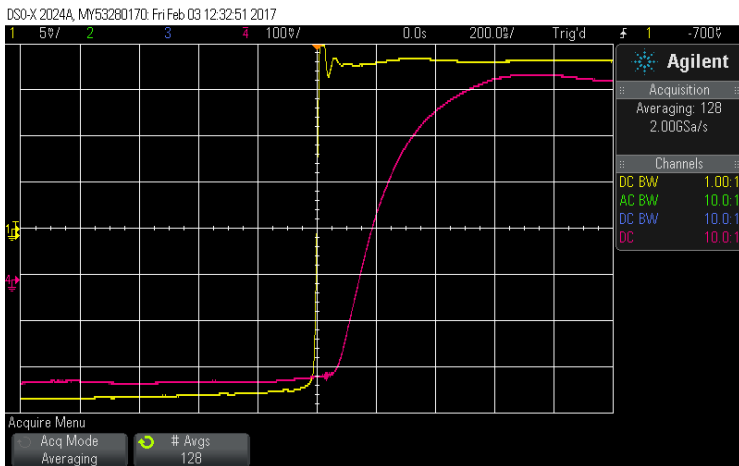


Figure 3.20: The response of the signal processing chain (red curve) to a large step-like input signal (yellow curve). The rise time of 200 ns from 0% to 50% can be inferred, indicating the -3 dB bandwidth of 5 MHz.

Therefore, the control input has been adjusted while observing the value of correlation with the developed tool. During these adjustments, values of correlation between 0 (corresponding to $\delta P' \sim \delta I$ extreme case, when the generated signal carries no information on laser voltage fluctuations) and ≈ 0.9 for the tested laser have been observed.

Finally, at the maximum signal correlation position, another control input (C3 on Figure 3.9) has been adjusted to the maximum gain value which did not cause oscillations in the feedback loop. A servo bump has been observed at 3 MHz, well corresponding to the previously measured value of the circuit bandwidth. The circuit performance in noise reduction measured with an optical frequency discriminator is demonstrated on Figure 3.22. A near-uniform 10 times frequency noise power spectral density reduction has been observed at Fourier frequencies between 1 kHz and 2 MHz (Figure 3.23), several times exceeding the bandwidth of the setup previously demonstrated in sec-

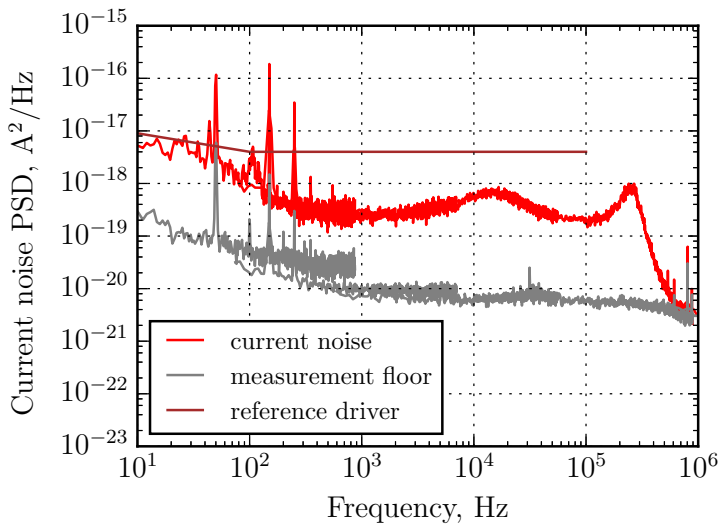


Figure 3.21: The current noise power spectral density of the constant current source part of the developed circuit (red) compared to the one of the reference commercial low noise current source (brown, approximate values from its datasheet). Noise floor of the measurement circuit is shown in grey.

tion 3.5.

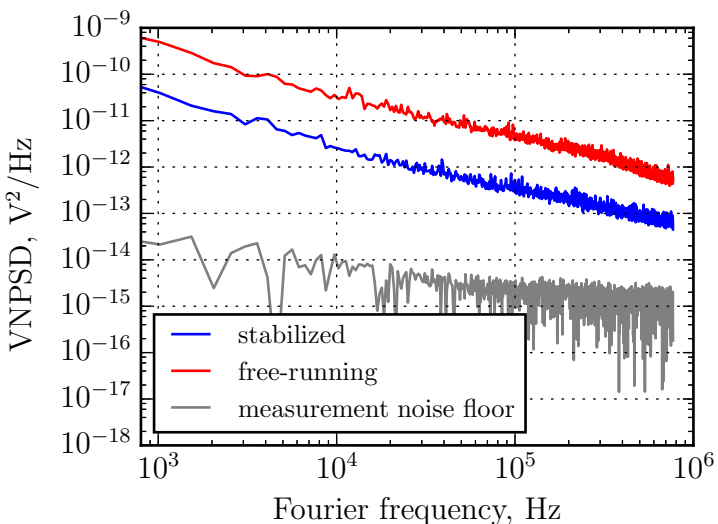


Figure 3.22: Voltage power spectral density noise measured on an optical detector registering frequency noise of a QCL in free-running and stabilized conditions. Measurement noise floor corresponds to a blocked optical beam condition.

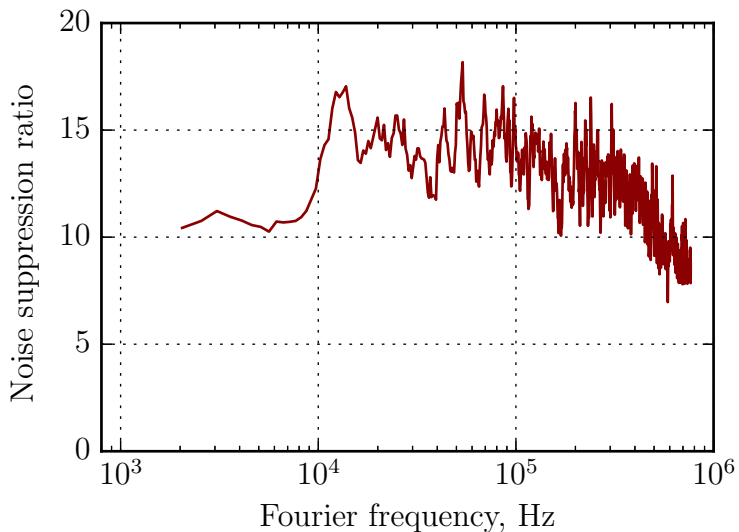


Figure 3.23: The ratio of suppression of frequency noise spectral density in a QCL driven by the developed driver. The measurement is obtained by dividing the red trace in Figure 3.22 by the blue one and applying a rolling-mean low-pass filter with a window of 8.

3.7 Conclusions on power stabilization

The principal limitation of the demonstrated noise reduction technique, as well as the one previously shown [82], arises from the imperfect correlation (≤ 0.9) between QCL voltage noise and frequency noise. As mentioned in [110], the reason behind the imperfect correlation might be that the generation of frequency noise takes place in the whole laser cavity and might be non-uniformly distributed, while the measured voltage fluctuations represent only an image averaged across the whole device. A further study, probably on devices with different geometries and dimensions, is required in order to understand the origin of this value and whether it can be improved in order to achieve tighter stabilization with the developed method.

Furthermore, a correlation between optical and electrical noise was also observed in traditional interband semiconductor lasers [105, 106], so the method could be used for stabilization of these devices, too.

3.8 Dual frequency QCLs

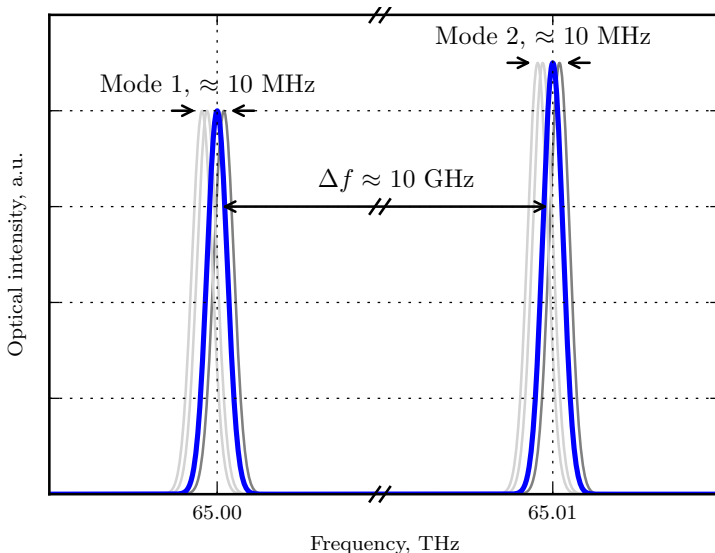


Figure 3.24: Principle of a dual frequency laser, illustrating the assumption that the frequency noise of the two modes is correlated.

3.8.1 Introduction

Quantum cascade lasers with *Distributed Feedback* (DFB) gratings or *Distributed Bragg Reflectors* (DBR) are typically designed for single-mode operation. However, this is not easy to achieve, and, above a certain output power, a dual-mode or few-mode optical spectrum is often observed (Figure 3.24). These modes are separated in the frequency domain by multiples of the *Free Spectral Range* (FSR) of the laser resonator. For a QCL with a typical chip length between 1 and 10 mm and a refractive index of ≈ 3 , the FSR lies between 5 and 50 GHz.

Lasers simultaneously operating at two wavelengths are attractive

for a number of applications, such as transmission of *Radio Frequency* (RF) signals over optical fibers [132, 133] or in free space [134], LIDAR [135], or RF generation [136, 137]. Their interest lies in the fact that they simultaneously provide an optical frequency (\approx 100 THz) and a radio frequency (\approx 10 GHz). A different approach to simultaneously transmit optical and RF signals in the mid-infrared is by amplitude modulation of a QCL. This can be achieved by a direct modulation of the laser current [138] or using a modulated external illumination of the QCL facet [139]. However, this comes at the price of an increased complexity.

A dual wavelength laser is more advantageous, as it naturally carries the desired RF signal. However, the dual-mode operation of a QCL has not been investigated so far, and a few questions remained open about its applicability, such as the achievable mode-spacing tunability and stability. Here, the first noise analysis and frequency stabilization of a dual-mode QCL are presented. A single-mode QCL has a typical linewidth in the MHz range [80], resulting from internal electrical fluctuations that induce temperature variations within the laser active region [111]. These temperature variations finally result in fluctuations of the QCL optical frequency. From the origin of these fluctuations, one can expect that they will perturb in a very similar way adjacent Fabry-Perot modes, for which dispersion is negligible compared to the situation of modes spaced by tens of cm^{-1} located on each side of the spectrum of a typical multi-mode QCL without a grating. If frequency fluctuations in dual-mode QCLs are indeed strongly correlated, one mode can be used to measure the instantaneous frequency of the other one and to stabilize both at the same time.

3.8.2 Laser fabrication

Dual-mode operation is typical for DFB QCLs [140, 141] due to the uncertainty in the cavity length resulting from the cleaving process

and to the possibility for a second mode to start lasing on the other side of the grating spectrum. In this work, a DBR design has been employed, which can also operate non-single-mode [142]. As illustrated in Figure 3.25, two Fabry-Perot modes close to the center of the grating spectrum can sense nearly the same reflectivity and lase, therefore, simultaneously.

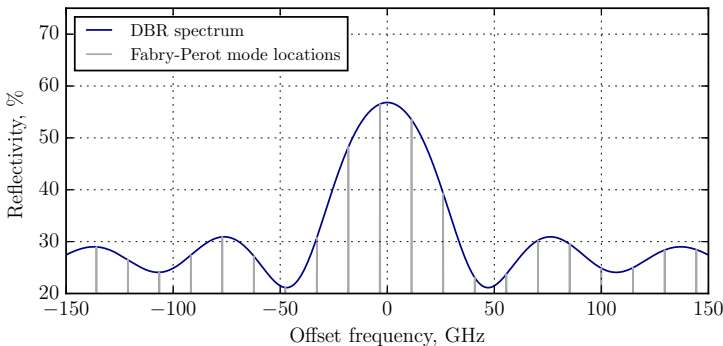


Figure 3.25: Reflectivity spectrum of a DBR (calculated as described in [143]) with the locations of the Fabry-Perot modes (grey lines) separated by the cavity FSR of ≈ 10 GHz.

The lasers designed to emit in the 4.6- μm range were processed in a buried heterostructure configuration with a ridge width of 9.0 μm . A distributed Bragg mirror section with a length of 0.75 mm and a grating period of 0.7515 μm were processed. Then a Fabry-Perot section was cleaved at a length of 3.75 mm (out of the grating), resulting in a total device length of 4.5 mm. A gold layer was deposited on top of the structure to form a single electrical contact, used to pump the two sections with a uniform current density. Both facets were left uncoated. The lasers were mounted epitaxial side up on copper submounts.

3.8.3 Characterization

QCLs capable of operating in a dual-mode regime have been selected and characterized. As a first step, standard LIV curves have been recorded and the emission spectrum has been measured at different operating currents using a FTIR spectrometer. In the selected QCL, a transition from single-mode to dual-mode emission occurs at room temperature (20°C) at a current of 740 mA. In comparison, the threshold current is 680 mA and the roll-over current 1050 mA (Figure 3.26). Only the light emitted from the front facet, corresponding to the Fabry-Perot section, has been considered in these measurements. In all subsequently presented data, the laser was operated at 20°C and within the current range of dual-mode operation.

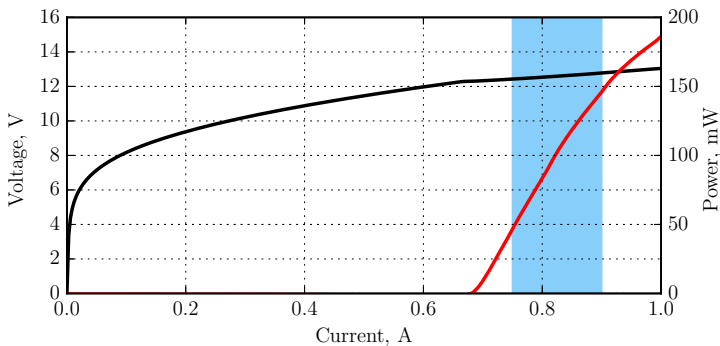


Figure 3.26: LIV curves of the selected QCL at 20°C . The blue area indicates the current range corresponding to a stable dual-mode operation.

Then, the stability of the dual-mode operation of the laser (absence of self-pulsations, self-frequency modulation, etc.) has been assessed by observing the emitted optical power using a fast photodiode (Vigo PVMI-4TE-8, 250 MHz bandwidth) connected to a digital oscilloscope. A first measurement was made on the total output power, showing 1.4×10^{-3} of relative Root Mean Square (RMS) noise. Then,

one of the two modes was filtered out by tuning it to a strong gas absorption line (a 10-cm gas cell filled with 2 mbar of N₂O was used for this purpose) and the optical power of the only remaining mode was detected, showing a relative RMS noise of 1.3×10^{-3} .

The exact spacing of the two optical modes has been investigated by detecting their RF beat-note that appears as an AC component in the laser current. This detection scheme described in [144] circumvents the need of a very fast detector (at least 12 GHz for the present laser) that would be required to optically detect the beat signal. The RF signal has been extracted from the QCL using a bias tee (Aeroflex 8800SMF-12). A special RF probe in the shape of a press contact was made to efficiently couple the weak RF signal from the laser standard copper mount into a coaxial cable (photos shown in Appendix A). The obtained signal was amplified using a low-noise broadband amplifier with a gain of 38 dB (Pasternack PE15A3259) and measured with an electrical spectrum analyzer (HP 70000 series).

At an observation time of 100 s (100 averages of a 1-s sweep), the linewidth of the RF signal is around 30 kHz (Figure 3.27), much narrower than the typical MHz range linewidth [80] of the optical modes. This is a first indication that the frequency noise of the two modes is highly correlated and cancels out in their beat signal. The measured beat frequency of 11.7 GHz corresponds to an effective resonator length of 4.1 mm assuming the refractive index ≈ 3.1 which indicates that the optical mode penetrates slightly into the grating section in accordance with [145]. The possibility to tune the frequency spacing between the two laser modes was investigated by measuring the beat-note frequency while changing the laser bias current (Figure 3.28). From these measurements, a tuning rate of 0.9 MHz/mA was assessed.

In order to further investigate the noise of the two modes and their correlation, two fast optical detectors and two optical frequency discriminators have been used allowing the independent and simultaneous measurement of the frequency noise of each mode i (Figure 3.29). The optical set-up is shown in Figure 3.30. The output beam of the

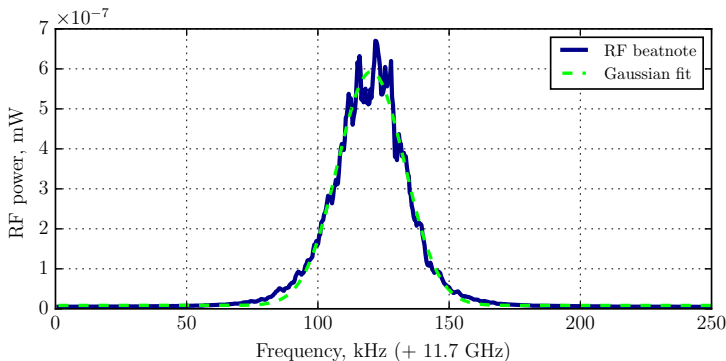


Figure 3.27: Electrical beatnote of a free-running dual wavelength QCL measured between its electrodes, averaged over 100 sweeps (100 s total observation time); resolution bandwidth: 1 kHz, measured linewidth: 30 kHz.

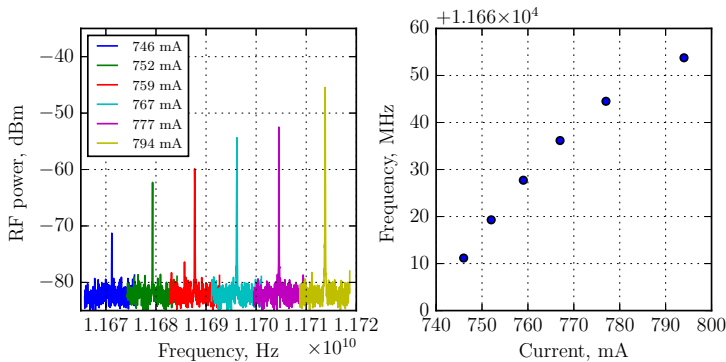


Figure 3.28: Continuous tuning of the frequency spacing between the two optical modes with the laser current. Left: recorded RF spectra at various currents; right: tuning curve extracted from the peak locations.

QCL was first split by a 50/50 beamsplitter after a collimating aspheric lens ($f = 1.873$ mm) and the two resultant beams were sent to two distinct frequency discriminators. The first discriminator was made of the aforementioned gas cell and had fixed absorption lines. The laser current was adjusted such that one mode was tuned to the side of a strong N₂O absorption line, where it got discriminated, i.e., the frequency fluctuations of this mode were converted into intensity fluctuations by the steep slope of the absorption line, and the resulting power fluctuations were detected by the photodiode in the cell transmission signal. The second mode was fully transmitted through the gas cell and also contributed to the photodiode signal, but only with its intensity noise, which was negligible compared to the converted frequency noise of the discriminated mode.

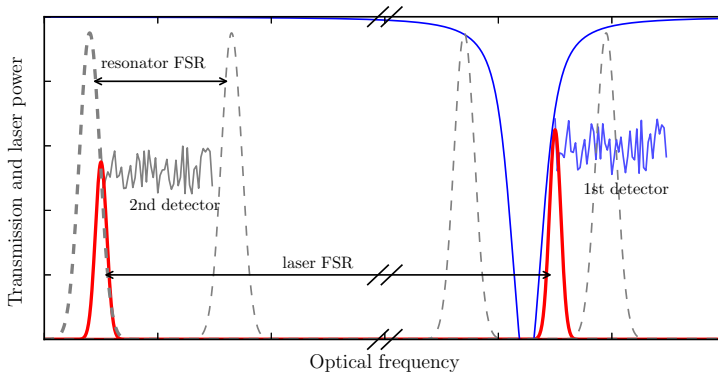


Figure 3.29: Scheme of principle of the simultaneous measurement of the frequency fluctuations of the two optical modes of the QCL using two distinct frequency discriminators: the frequency noise of the first laser mode (red peak on the right) is discriminated by a gas absorption line (shown in solid blue), whereas the noise of the second one (red peak on the left) by an optical resonator (shown in dashed grey). The respective linewidths are not to scale for illustrative purpose.

In the second arm, a tunable frequency discriminator was required to

be able to discriminate the second mode. A scanning Fabry-Perot interferometer of medium finesse (1-GHz FSR, 5-MHz resonance width) was used for this purpose. An additional lens with a focal length $f = 100$ mm was used for mode matching, and optical feedback from the cavity towards the laser was reduced to a non-disturbing level by inserting a reflective attenuator in this branch. A second slightly different photodiode (Vigo PVI-4TE-8) measured the light transmitted through the resonator. The Fabry-Perot resonator was tuned via a *Piezoelectric Transducer* (PZT) holding one of the cavity mirrors in order that the second QCL mode was located on the side of a resonance, approximately at its half height.

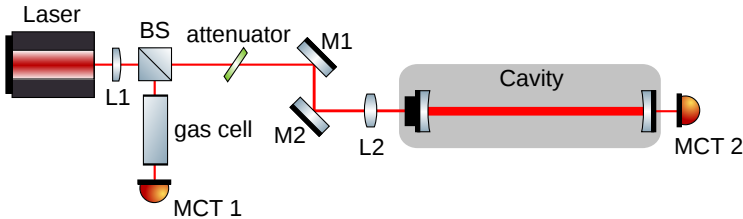


Figure 3.30: Experimental workbench. M1, M2 – mirrors, L1, L2 – lenses with 1.87 mm and 100 mm focal lengths, BS – non-polarizing beam splitter, MCT 1, MCT 2 – fast optical detectors.

With these two optical frequency discriminators, two independent signals were obtained, each of them measuring the instantaneous frequency of one of the modes. For verification and calibration, the resonator was first tuned such that the same laser mode was discriminated in both optical branches (i.e., by the gas absorption line and the Fabry-Perot resonance). The electrical signals of both optical detectors were recorded by a fast digital oscilloscope at 10 ns resolution (Figure 3.31). Both signals were filtered by a first order digital low-pass filter with a -3 dB cut-off frequency of 200 kHz in order to compensate for the different frequency response of the discriminators. The Pearson correlation coefficient $R = 0.98$ calculated for the two normalized signals proves the equivalence of the two consid-

ered discriminators. Then, the resonator was tuned so that the two optical branches discriminated different laser modes and the value of $R = 0.96$ was found, confirming the high correlation between the frequency fluctuations of the two optical modes (Figure 3.31).

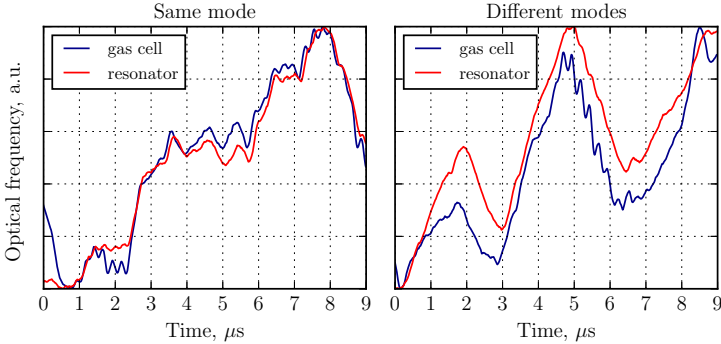


Figure 3.31: Left: instantaneous frequency of the same optical mode discriminated with both the gas cell (blue curve) and the optical resonator (red curve): $R = 0.98$. Right: instantaneous frequencies of the two different modes simultaneously observed with the two optical discriminators: $R = 0.96$.

3.8.4 Stabilization

We have used a side-of-fringe locking method to stabilize one of the two laser modes to a N₂O absorption line and studied the resulting behavior of the second mode. As a result of high correlation between the instantaneous optical frequency of the two modes shown in the previous experiment, this stabilization is expected to lead to a simultaneous locking of the second mode. A PI (proportional-integral) controller was added to the aforementioned setup and the absorption spectroscopy signal offset by a controlled voltage was used as an input error signal. The output signal of the PI controller was applied as feedback to the laser current.

As a first qualitative evaluation of this stabilization, a resonance of the Fabry-Perot cavity has been scanned in the second optical branch through one or the other QCL mode, when the laser was free-running or stabilized to the gas absorption line in the first optical branch. Figure 3.32 shows the corresponding results. The two modes are clearly identified by their slightly different amplitude, with a ratio of $\approx 1.2 : 1$ in these conditions. When the slightly weaker mode (left plot) was directly stabilized to the gas absorption line, the stronger one (right plot) experienced a clear noise reduction, despite it was not directly locked to an optical reference. This confirms the assumption of the noise correlation between the two modes. In the stabilized case, the width of the observed spectra corresponds to the linewidth of the Fabry-Perot resonance (≈ 5 MHz), as the laser linewidth becomes narrower as a result of the noise reduction (Figure 3.32).

For a more quantitative evaluation of the effect of the stabilization on the two optical modes, their frequency noise power spectral density has been determined in free-running and locked conditions. It was measured by acquiring frequency noise traces in time domain, and then applying Welch's periodogram method [76]. As in the free-running case, the laser was not locked to a specific point on an absorption line or resonator line, it experienced slow periodic frequency drifts with variation of external temperature. Therefore, the oscilloscope traces have been recorded continuously, but only the ones with a correct mean level of signal, corresponding to the position of the steepest slope of the frequency discrimination characteristic of the absorption line, were taken into account. Figure 3.33 shows a similar noise reduction for the two modes. The values of linewidths at 1 ms observation time estimated from those plots according to [77] are: 406 kHz free-running and 65 kHz locked for the directly locked mode resulting in 6.2 times reduction; 380 kHz free-running and 70 kHz locked for the indirectly locked mode resulting in 5.4 times reduction.

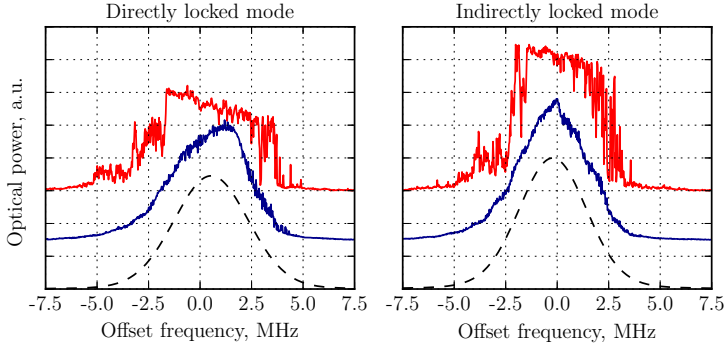


Figure 3.32: Profiles of the two modes of a dual wavelength QCL measured with a tunable Fabry-Perot resonator during a piezo scan for the free-running (red) and stabilized (blue) QCL, along with a Gaussian fit (dashed black). The mode on the left was used in the stabilization.

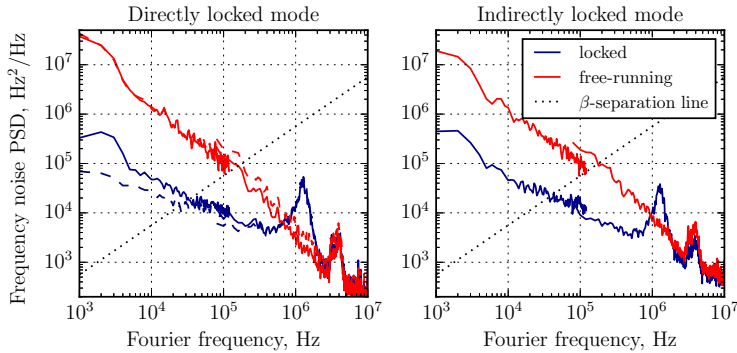


Figure 3.33: Frequency noise power spectral density of both modes measured with the optical resonator, in the free-running (red) and stabilized (blue) cases. The dashed lines show corresponding spectra obtained from the gas cell discriminator branch, available for one mode only. The β -separation line is used for linewidth estimation [77].

3.8.5 Conclusions

This part of work presents the study of frequency relations in Quantum Cascade Lasers operating at two wavelength simultaneously. They demonstrate excellent stability of intermodal spacing, which is important for applications and general understanding of multi-mode operation of QCLs. Dual wavelength lasers can be made more flexible in terms of tuning by use of more complicated gratings [146–148] or RF injection [149–151]. Compared to optical frequency combs, which also link optical and RF frequency domains, dual frequency lasers are narrower spectrally, have broader intermode beatnote [152], but have much more optical power per mode, which for some applications is advantageous. A further study, for example – a direct phase noise measurement of the beatnote signal or a measurement of correlation between instant frequencies of the beatnote and one of the optical modes, is required to understand the limits of stability of the intermodal frequency spacing. It will also allow to put the dual frequency QCLs into a direct comparison with other existing photonic RF signal generators, such as the ones based on stimulated Brillouin scattering in optical fibers [153] or Kerr frequency comb oscillators utilizing whispering gallery mode microresonators [154]. At first glance, dual frequency QCLs demonstrate significantly wider beatnotes (kHz-level compared to Hz-level of mentioned competitors), but have advantages of being tighter integrated (e.g. not requiring any external optical elements for local RF generation) and operating in mid-infrared spectral region, which is, for instance, preferred to near-infrared for free-space transmission of light [134]. Another interesting possibility would be to check if the absolute stability of the optical modes can be improved by locking the RF beatnote to another stable source, as described in [155].

Another interesting and simple to implement scheme of use of a dual-frequency QCL would make use of two gas cells at slightly different pressures: whereas the lower-pressure gas cell would serve to lock one of the laser modes to some absorption line, the higher-pressure one

would filter the same mode completely from the output (due to larger width of the same absorption line). This would result in an absolutely-referenced narrow-line single-mode laser source at a wavelength, not easily available for other simple stabilization methods such as direct [83] or offset [20] locking.

4

Conclusions

This work presents the research steps towards high power and narrow linewidth quantum cascade lasers. The demonstrated results provide a general understanding of the observed phenomena as well as practically useful solutions employing them.

The gain-guided lasers have demonstrated high levels of output power together with high beam quality; they are interesting to be tested in external cavity configuration which might even further improve their qualities. The corresponding results have been published in Optics Express [156]. These lasers [157] and high power pulsed drivers [158] have already become commercial products available from Alpes Lasers SA.

The concept of power stabilization was first demonstrated in a digital implementation published in Optics Letters [159] and later integrated into the analog one, closer to be a scientific instrument. This second design is being prepared to be patented. Having been demonstrated on QCLs, this principle of stabilization is worth being tested in other applications, for example diode lasers, which also generate observable electronic noise influencing their operation.

The dual frequency QCLs with their characterized stability and possi-

bility of mode tuning are interesting to test in applications requiring a link between RF and optical frequencies, in particular absolutely referenced precision spectroscopy. Another interesting direction of their development would be to extend the possibility of tuning of their mode spacing without degrading its stability. A part of work on these lasers has been submitted as a research paper.

Bibliography

- [1] Kazarinov, R. and Suris, R. Possible Amplification of Electromagnetic Waves in a Semiconductor with a Superlattice. *Fizika i Tekhnika Poluprovodnikov*, 5(4):797–800 (1971).
- [2] Faist, J., Capasso, F., Sivco, D. L., Sirtori, C., Hutchinson, A. L., and Cho, A. Y. Quantum Cascade Laser. *Science*, 264(5158):553–556 (1994).
- [3] Li, L., Chen, L., Zhu, J., Freeman, J., Dean, P., Valavanis, A., Davies, A. G., and Linfield, E. H. Terahertz Quantum Cascade Lasers with >1 W Output Powers. *Electronics Letters*, 50(4):309–311 (2014).
- [4] Faist, J. *Quantum Cascade Lasers*. OUP Oxford (2013).
- [5] Valavanis, A., Grier, A., Cooper, J. D., Evans, C. A., and Harrison, P. Quantum Wells, Wires and Dots (QWWAD): Free and Open-Source Simulation Tools for Intersubband Devices. *The 13th International Conference on Intersubband Transitions in Quantum Wells* (2015).
- [6] Harrison, P. and Valavanis, A. *Quantum Wells, Wires and Dots: Theoretical and Computational Physics of Semiconductor Nanostructures*. John Wiley & Sons, Inc, West Sussex, United Kingdom ; Hoboken, NJ, fourth edition edition (2016).

- [7] Cathabard, O., Teissier, R., Devenson, J., Moreno, J. C., and Baranov, A. N. Quantum Cascade Lasers Emitting near 2.6 μm . *Applied Physics Letters*, 96(14):141110 (2010).
- [8] Walther, C., Fischer, M., Scalari, G., Terazzi, R., Hoyler, N., and Faist, J. Quantum Cascade Lasers Operating from 1.2 to 1.6 THz. *Applied Physics Letters*, 91(13):131122 (2007).
- [9] Yamanishi, M., Hirohata, T., Bartalini, S., and De Natale, P. Quantum-Cascade Lasers: Line-Narrowing and Suppression of Flicker-Noise. In *OptoElectronics and Communications Conference (OECC) Held Jointly with 2016 International Conference on Photonics in Switching (PS), 2016 21st*, pages 1–3. IEEE (2016).
- [10] Rösch, M., Scalari, G., Beck, M., and Faist, J. Octave-Spanning Semiconductor Laser. *Nature Photonics*, 9(1):42–47 (2014).
- [11] Hugi, A., Villares, G., Blaser, S., Liu, H. C., and Faist, J. Mid-Infrared Frequency Comb Based on a Quantum Cascade Laser. *Nature*, 492(7428):229–233 (2012).
- [12] Bismuto, A., Bidaux, Y., Tardy, C., Terazzi, R., Gresch, T., Wolf, J., Blaser, S., Muller, A., and Faist, J. Extended Tuning of Mid-Ir Quantum Cascade Lasers Using Integrated Resistive Heaters. *Optics Express*, 23(23):29715 (2015).
- [13] Maulini, R., Yarekha, D. A., Bulliard, J.-M., Giovannini, M., Faist, J., and Gini, E. Continuous-Wave Operation of a Broadly Tunable Thermoelectrically Cooled External Cavity Quantum-Cascade Laser. *Optics letters*, 30(19):2584–2586 (2005).
- [14] Lyakh, A., Maulini, R., Tsekoun, A., Go, R., and Patel, C. K. N. Tapered 4.7 μm Quantum Cascade Lasers with Highly Strained Active Region Composition Delivering over 4.5 Watts of Continuous Wave Optical Power. *Optics Express*, 20(4):4382–4388 (2012).

- [15] Bai, Y., Bandyopadhyay, N., Tsao, S., Slivken, S., and Razeghi, M. Room Temperature Quantum Cascade Lasers with 27% Wall Plug Efficiency. *Applied Physics Letters*, 98(18):181102 (2011).
- [16] Heydari, D., Bai, Y., Bandyopadhyay, N., Slivken, S., and Razeghi, M. High Brightness Angled Cavity Quantum Cascade Lasers. *Applied Physics Letters*, 106(9):091105 (2015).
- [17] Borri, S. and Santambrogio, G. Laser Spectroscopy of Cold Molecules. *Advances in Physics: X*, 1(3):368–386 (2016).
- [18] Germann, M., Tong, X., and Willitsch, S. Observation of Electric-Dipole-Forbidden Infrared Transitions in Cold Molecular Ions. *Nature Physics*, 10(11):820–824 (2014).
- [19] Germann, M. *Dipole-Forbidden Vibrational Transitions in Molecular Ions*. Ph.D. thesis, Basel (2016).
- [20] Bielsa, F., Douillet, A., Valenzuela, T., Karr, J.-P., and Hilico, L. Narrow-Line Phase-Locked Quantum Cascade Laser in the $9.2\text{ }\mu\text{m}$ Range. *Optics Letters*, 32(12):1641–1643 (2007).
- [21] Bielsa, F., Djerroud, K., Goncharov, A., Douillet, A., Valenzuela, T., Daussy, C., Hilico, L., and Amy-Klein, A. HCOOH High-Resolution Spectroscopy in the $9.18\mu\text{m}$ Region. *Journal of Molecular Spectroscopy*, 247(1):41–46 (2008).
- [22] Karr, J.-P., Hilico, L., and Korobov, V. I. Theoretical Progress in the H_2^+ Molecular Ion: Towards Electron to Proton Mass Ratio determinationThis Paper Was Presented at the International Conference on Precision Physics of Simple Atomic Systems, Held at École de Physique, Les Houches, France, 30 May – 4 June, 2010. *Canadian Journal of Physics*, 89(1):103–107 (2011).
- [23] Schiller, S., Kortunov, I., M. Hernández, V., and Gianturco, F. Quantum State Preparation of Homonuclear Molecular Ions

- Enabled via a Cold Buffer Gas: An Ab Initio Study for the H₂+ and the D₂+ Case. *Physical Review A* (2017).
- [24] Santamaria, L., Di Sarno, V., Ricciardi, I., Mosca, S., De Rosa, M., Santambrogio, G., Maddaloni, P., and De Natale, P. Assessing the Time Constancy of the Proton-to-Electron Mass Ratio by Precision Ro-Vibrational Spectroscopy of a Cold Molecular Beam. *Journal of Molecular Spectroscopy*, 300:116–123 (2014).
 - [25] Fasci, E., Coluccelli, N., Cassinerio, M., Gambetta, A., Hilico, L., Gianfrani, L., Laporta, P., Castrillo, A., and Galzerano, G. Narrow-Linewidth Quantum Cascade Laser at 8.6 μm . *Optics Letters*, 39(16):4946 (2014).
 - [26] Versolato, O. O., Schwarz, M., Hansen, A. K., Gingell, A. D., Windberger, A., Kłosowski, Ł., Ullrich, J., Jensen, F., Crespo López-Urrutia, J. R., and Drewsen, M. Decay Rate Measurement of the First vibrationally Excited State of MgH + in a Cryogenic Paul Trap. *Physical Review Letters*, 111(5) (2013).
 - [27] Paschke, K., Liu, P. Q., Michel, A. P., Smith, J., Moshary, F., and Gmachl, C. Quantum Cascade Laser for Elastic-Backscattering LIDAR Measurement. In *Conference on Lasers and Electro-Optics*, pages 1–2. Optical Society of America (2010).
 - [28] Maulini, R., Lyakh, A., Tsekoun, A. G., Go, R., Lane, M., Macdonald, T., and Patel, C. K. N. High Power, High Efficiency Quantum Cascade Laser Systems for Directional Infrared Countermeasures and Other Defense and Security Applications. In *Technologies for Optical Countermeasures VI*, volume 7483, pages 74830D1–9 (2009).
 - [29] Maulini, R., Lyakh, A., Tsekoun, A., and Patel, C. K. N. $\lambda \sim 7.1 \mu\text{m}$ Quantum Cascade Lasers with 19% Wall-Plug Efficiency at Room Temperature. *Optics Express*, 19(18):17203–17211 (2011).

- [30] Lyakh, A., Suttinger, M., Go, R., Figueiredo, P., and Todi, A. $5.6\text{ }\mu\text{m}$ Quantum Cascade Lasers Based on a Two-Material Active Region Composition with a Room Temperature Wall-Plug Efficiency Exceeding 28%. *Applied Physics Letters*, 109(12):121109 (2016).
- [31] Faist, J. Wallplug Efficiency of Quantum Cascade Lasers: Critical Parameters and Fundamental Limits. *Applied Physics Letters*, 90(25):253512 (2007).
- [32] Liu, H. C., Buchanan, M., and Wasilewski, Z. R. How Good Is the Polarization Selection Rule for Intersubband Transitions? *Applied Physics Letters*, 72(14):1682–1684 (1998).
- [33] Ahn, S., Ristanic, D., Gansch, R., Reininger, P., Schwarzer, C., MacFarland, D. C., Detz, H., Schrenk, W., and Strasser, G. Quantum Cascade Lasers with a Tilted Facet Utilizing the Inherent Polarization Purity. *Optics Express*, 22(21):26294 (2014).
- [34] Colombelli, R., Capasso, F., Gmachl, C., Hutchinson, A. L., Sivco, D. L., Tredicucci, A., Wanke, M. C., Sergent, A. M., and Cho, A. Y. Far-Infrared Surface-Plasmon Quantum-Cascade Lasers at $21.5\text{ }\mu\text{m}$ and $24\text{ }\mu\text{m}$ Wavelengths. *Applied Physics Letters*, 78(18):2620–2622 (2001).
- [35] Sirtori, C., Gmachl, C., Capasso, F., Faist, J., Sivco, D. L., Hutchinson, A. L., and Cho, A. Y. Long-Wavelength ($\lambda \approx 8 - 11.5\mu\text{m}$) Semiconductor Lasers with Waveguides Based on Surface Plasmons. *Optics letters*, 23(17):1366–1368 (1998).
- [36] Moreau, V., Bahriz, M., Palomo, J., Wilson, L. R., Krysa, A. B., Sirtori, C., Austin, D. A., Cockburn, J. W., Roberts, J. S., and Colombelli, R. Optical Mode Control of Surface-Plasmon Quantum Cascade Lasers. *IEEE Photonics Technology Letters*, 18(23):2499–2501 (2006).
- [37] Casey, H. *Heterostructure Lasers*. Elsevier Science (2012).

- [38] Bai, Y., Slivken, S., Darvish, S. R., Haddadi, A., Gokden, B., and Razeghi, M. High Power Broad Area Quantum Cascade Lasers. *Applied Physics Letters*, 95(22):221104 (2009).
- [39] Ahn, S., Schwarzer, C., Zederbauer, T., MacFarland, D. C., Detz, H., Andrews, A. M., Schrenk, W., and Strasser, G. High-Power, Low-Lateral Divergence Broad Area Quantum Cascade Lasers with a Tilted Front Facet. *Applied Physics Letters*, 104(5):051101 (2014).
- [40] Lerttamrab, M., Chuang, S. L., Gmachl, C., Sivco, D. L., Capasso, F., and Cho, A. Y. Linewidth Enhancement Factor of a Type-I Quantum-Cascade Laser. *Journal of Applied Physics*, 94(8):5426 (2003).
- [41] Aellen, T., Maulini, R., Terazzi, R., Hoyler, N., Giovannini, M., Faist, J., Blaser, S., and Hvozdara, L. Direct Measurement of the Linewidth Enhancement Factor by Optical Heterodyning of an Amplitude-Modulated Quantum Cascade Laser. *Applied Physics Letters*, 89(9):091121 (2006).
- [42] Hess, O., Koch, S. W., and Moloney, J. V. Filamentation and Beam Propagation in Broad-Area Semiconductor Lasers. *IEEE journal of quantum electronics*, 31(1):35–43 (1995).
- [43] Marciante, J. R. and Agrawal, G. P. Nonlinear Mechanisms of Filamentation in Broad-Area Semiconductor Lasers. *IEEE Journal of Quantum Electronics*, 32(4):590–596 (1996).
- [44] Marciante, J. R. and Agrawal, G. P. Spatio-Temporal Characteristics of Filamentation in Broad-Area Semiconductor Lasers: Experimental Results. *IEEE Photonics Technology Letters*, 10(1):54–56 (1998).
- [45] Bai, Y., Slivken, S., Lu, Q. Y., Bandyopadhyay, N., and Razeghi, M. Angled Cavity Broad Area Quantum Cascade Lasers. *Applied Physics Letters*, 101(8):081106 (2012).

- [46] Friedli, P., Sigg, H., Hinkov, B., Hugi, A., Riedi, S., Beck, M., and Faist, J. Four-Wave Mixing in a Quantum Cascade Laser Amplifier. *Applied Physics Letters*, 102(22):222104 (2013).
- [47] Gordon, A., Wang, C. Y., Diehl, L., Kärtner, F. X., Belyanin, A., Bour, D., Corzine, S., Höfler, G., Liu, H. C., Schneider, H., Maier, T., Troccoli, M., Faist, J., and Capasso, F. Multimode Regimes in Quantum Cascade Lasers: From Coherent Instabilities to Spatial Hole Burning. *Physical Review A*, 77(5) (2008).
- [48] Choi, H., Diehl, L., Wu, Z.-K., Giovannini, M., Faist, J., Capasso, F., and Norris, T. B. Gain Recovery Dynamics and Photon-Driven Transport in Quantum Cascade Lasers. *Physical Review Letters*, 100(16) (2008).
- [49] Yu, N., Diehl, L., Cubukcu, E., Bour, D., Corzine, S., Höfler, G., Wojcik, A. K., Crozier, K. B., Belyanin, A., and Capasso, F. Coherent Coupling of Multiple Transverse Modes in Quantum Cascade Lasers. *Physical Review Letters*, 102(1) (2009).
- [50] Yang, Q., Kinzer, M., Fuchs, F., Hugger, S., Hinkov, B., Bronner, W., Lösch, R., Aidam, R., and Wagner, J. Beam Steering and Lateral Hole Burning in Mid-Infrared Quantum-Cascade Lasers. *physica status solidi (c)*, 9(2):302–305 (2012).
- [51] Gresch, T., Giovannini, M., Hoyer, N., and Faist, J. Quantum Cascade Lasers with Large Optical Waveguides. *IEEE Photonics Technology Letters*, 18(3):544–546 (2006).
- [52] Semtsiv, M. P. and Masselink, W. T. Above Room Temperature Continuous Wave Operation of a Broad-Area Quantum-Cascade Laser. *Applied Physics Letters*, 109(20):203502 (2016).
- [53] Siegman, A. E. How to (Maybe) Measure Laser Beam Quality. *Optical Society of America Annual Meeting 1997* (1998).

- [54] Krishnaswami, K., Bernacki, B. E., Cannon, B. D., Ho, N., and Anheier, N. C. Emission and Propagation Properties of Mid-infrared Quantum Cascade Lasers. *IEEE Photonics Technology Letters*, 20(4):306–308 (2008).
- [55] Kirch, J. D., Chang, C.-C., Boyle, C., Mawst, L. J., Lindberg, D., Earles, T., and Botez, D. 5.5 W near-Diffraction-Limited Power from Resonant Leaky-Wave Coupled Phase-Locked Arrays of Quantum Cascade Lasers. *Applied Physics Letters*, 106(6):061113 (2015).
- [56] Botez, D., Mawst, L. J., and Peterson, G. Resonant Leaky-Wave Coupling in Linear Arrays of Antiguides. *Electronics Letters*, 24(21):1328–1330 (1988).
- [57] Wen, J., Zhang, Y., and Xiao, M. The Talbot Effect: Recent Advances in Classical Optics, Nonlinear Optics, and Quantum Optics. *Advances in Optics and Photonics*, 5(1):83 (2013).
- [58] Leger, J. R. Lateral Mode Control of an AlGaAs Laser Array in a Talbot Cavity. *Applied Physics Letters*, 55(4):334–336 (1989).
- [59] Wang, L., Zhang, J., Jia, Z., Zhao, Y., Liu, C., Liu, Y., Zhai, S., Ning, Z., Xu, X., and Liu, F. Phase-Locked Array of Quantum Cascade Lasers with an Integrated Talbot Cavity. *Optics Express*, 24(26):30275 (2016).
- [60] Meng, B., Qiang, B., Rodriguez, E., Hu, X. N., Liang, G., and Wang, Q. J. Coherent Emission from Integrated Talbot-Cavity Quantum Cascade Lasers. *Optics Express*, 25(4):3077 (2017).
- [61] Bai, Y., Darvish, S. R., Slivken, S., Sung, P., Nguyen, J., Evans, A., Zhang, W., and Razeghi, M. Electrically Pumped Photonic Crystal Distributed Feedback Quantum Cascade Lasers. *Applied Physics Letters*, 91(14):141123 (2007).
- [62] Gökden, B., Bai, Y., Bandyopadhyay, N., Slivken, S., and Razeghi, M. Broad Area Photonic Crystal Distributed Feed-

- back Quantum Cascade Lasers Emitting 34 W at $\lambda \sim 4.36 \mu\text{m}$. *Applied Physics Letters*, 97(13):131112 (2010).
- [63] Bai, Y., Gokden, B., Darvish, S. R., Slivken, S., and Razeghi, M. Photonic Crystal Distributed Feedback Quantum Cascade Lasers with 12 W Output Power. *Applied Physics Letters*, 95(3):031105 (2009).
- [64] Peretti, R., Liverini, V., Siess, M. J., Liang, Y., Vigneron, P.-B., Wolf, J. M., Bonzon, C., Bismuto, A., Metaferia, W., Balaji, M., Lourdudoss, S., Gini, E., Beck, M., and Faist, J. Room Temperature Operation of a Deep Etched Buried Heterostructure Photonic Crystal Quantum Cascade Laser: Room Temperature Operation. *Laser & Photonics Reviews* (2016).
- [65] Salin, F. and Squier, J. Gain Guiding in Solid-State Lasers. *Optics Letters*, 17(19):1352–1354 (1992).
- [66] Polyanskiy, M. N. Refractive Index Database. <http://refractiveindex.info/> (2017).
- [67] Siklitsky, V. New Semiconductor Materials. Characteristics and Properties. <http://www.ioffe.ru/SVA/NSM/> (2001).
- [68] Lyakh, A., Zory, P., Wasserman, D., Shu, G., Gmachl, C., D’Souza, M., Botez, D., and Bour, D. Narrow Stripe-Width, Low-Ridge High Power Quantum Cascade Lasers. *Applied Physics Letters*, 90(14):141107 (2007).
- [69] Terazzi, R. and Faist, J. A Density Matrix Model of Transport and Radiation in Quantum Cascade Lasers. *New Journal of Physics*, 12(3):033045 (2010).
- [70] Okamoto, K. *Fundamentals of Optical Waveguides*. Electronics & Electrical. Elsevier (2006). LCCB: 2005051978.
- [71] Fathololoumi, S., Dupont, E., Razavipour, S., Laframboise, S., Delage, A., Wasilewski, Z., Bezingier, A., Rafi, G., Safavi-

- Naeini, S., Ban, D., and others. Electrically Switching Transverse Modes in High Power THz Quantum Cascade Lasers. *Optics express*, 18(10):10036–10048 (2010).
- [72] Faist, K., Hofstetter, D., Beck, M., Aellen, T., Rochat, M., and Blaser, S. Bound-to-Continuum and Two-Phonon Resonance, Quantum-Cascade Lasers for High Duty Cycle, High-Temperature Operation. *IEEE Journal of Quantum Electronics*, 38(6):533–546 (2002).
- [73] Bismuto, A., Blaser, S., Terazzi, R., Gresch, T., and Muller, A. High Performance, Low Dissipation Quantum Cascade Lasers across the Mid-IR Range. *Optics Express*, 23(5):5477 (2015).
- [74] Buijs, M., Tijburg, R., Haberern, K., and Gaines, J. Thermal Index Guiding in Gain-Guided Blue-Green II-VI Semiconductor Lasers. *Journal of Applied Physics*, 79(2):578 (1996).
- [75] Directed Energy Inc. PCO-7120 Laser Diode Driver Module Installation and Operation Notes (2003).
- [76] Welch, P. The Use of Fast Fourier Transform for the Estimation of Power Spectra: A Method Based on Time Averaging over Short, Modified Periodograms. *IEEE Transactions on Audio and Electroacoustics*, AU-15(2):70–73 (1967).
- [77] Di Domenico, G., Schilt, S., and Thomann, P. Simple Approach to the Relation between Laser Frequency Noise and Laser Line Shape. *Applied Optics*, 49(25):4801–4807 (2010).
- [78] Bucalovic, N., Dolgovskiy, V., Schori, C., Thomann, P., Di Domenico, G., and Schilt, S. Experimental Validation of a Simple Approximation to Determine the Linewidth of a Laser from Its Frequency Noise Spectrum. *Applied optics*, 51(20):4582–4588 (2012).
- [79] Mills, A. A., Gatti, D., Jiang, J., Mohr, C., Mefford, W., Gianfrani, L., Fermann, M., Hartl, I., and Marangoni, M. Coher-

- ent Phase Lock of a $9\ \mu\text{m}$ Quantum Cascade Laser to a $2\ \mu\text{m}$ Thulium Optical Frequency Comb. *Optics Letters*, 37(19):4083–4085 (2012).
- [80] Tombez, L., Di Francesco, J., Schilt, S., Di Domenico, G., Faist, J., Thomann, P., and Hofstetter, D. Frequency Noise of Free-Running $4.6\ \mu\text{m}$ Distributed Feedback Quantum Cascade Lasers near Room Temperature. *Optics Letters*, 36(16):3109–3111 (2011).
- [81] Cardilli, M. C., Dabbicco, M., Mezzapesa, F. P., and Scamarcio, G. Linewidth Measurement of Mid Infrared Quantum Cascade Laser by Optical Feedback Interferometry. *Applied Physics Letters*, 108(3):031105 (2016).
- [82] Tombez, L., Schilt, S., Hofstetter, D., and Südmeyer, T. Active Linewidth-Narrowing of a Mid-Infrared Quantum Cascade Laser without Optical Reference. *Optics Letters*, 38(23):5079 (2013).
- [83] Williams, R. M., Kelly, J. F., Hartman, J. S., Sharpe, S. W., Taubman, M. S., Hall, J. L., Capasso, F., Gmachl, C., Sivco, D. L., Baillargeon, J. N., and Cho, A. Y. Kilohertz Linewidth from Frequency-Stabilized Mid-Infrared Quantum Cascade Lasers. *Optics Letters*, 24(24):1844–1846 (1999).
- [84] Bartalini, S., Borri, S., Cancio, P., Castrillo, A., Galli, I., Giustfredi, G., Mazzotti, D., Gianfrani, L., and De Natale, P. Observing the Intrinsic Linewidth of a Quantum-Cascade Laser: Beyond the Schawlow-Townes Limit. *Physical Review Letters*, 104(8) (2010).
- [85] Cendejas, R. A., Phillips, M. C., Myers, T. L., and Taubman, M. S. Single-Mode, Narrow-Linewidth External Cavity Quantum Cascade Laser through Optical Feedback from a Partial-Reflector. *Optics Express*, 18(25):26037–26045 (2010).

- [86] Borri, S., Galli, I., Cappelli, F., Bismuto, A., Bartalini, S., Cancio, P., Giusfredi, G., Mazzotti, D., Faist, J., and De Natale, P. Direct Link of a Mid-Infrared QCL to a Frequency Comb by Optical Injection. *Optics Letters*, 37(6):1011–1013 (2012).
- [87] Rothman, L., Gordon, I., Barbe, A., Benner, D., Bernath, P., Birk, M., Boudon, V., Brown, L., Campargue, A., Champion, J.-P., Chance, K., Coudert, L., Dana, V., Devi, V., Fally, S., Flaud, J.-M., Gamache, R., Goldman, A., Jacquemart, D., Kleiner, I., Lacome, N., Lafferty, W., Mandin, J.-Y., Massie, S., Mikhailenko, S., Miller, C., Moazzen-Ahmadi, N., Naumenko, O., Nikitin, A., Orphal, J., Perevalov, V., Perrin, A., Predoi-Cross, A., Rinsland, C., Rotger, M., Šimečková, M., Smith, M., Sung, K., Tashkun, S., Tennyson, J., Toth, R., Vandaele, A., and Vander Auwera, J. The HITRAN 2008 Molecular Spectroscopic Database. *Journal of Quantitative Spectroscopy and Radiative Transfer*, 110(9-10):533–572 (2009).
- [88] Hitran on the Web. <http://hitran.iao.ru/> (2017).
- [89] Drever, R. W. P., Hall, J. L., Kowalski, F. V., Hough, J., Ford, G. M., Munley, A. J., and Ward, H. Laser Phase and Frequency Stabilization Using an Optical Resonator. *Applied Physics B*, 31(2):97–105 (1983).
- [90] Black, E. D. An Introduction to Pound–Drever–Hall Laser Frequency Stabilization. *American Journal of Physics*, 69(1):79–87 (2001).
- [91] Taubman, M. S., Myers, T. L., Cannon, B. D., Williams, R. M., Capasso, F., Gmachl, C., Sivco, D. L., and Cho, A. Y. Frequency Stabilization of Quantum-Cascade Lasers by Use of Optical Cavities. *Optics Letters*, 27(24):2164–2166 (2002).
- [92] Galli, I., Siciliani de Cumis, M., Cappelli, F., Bartalini, S., Mazzotti, D., Borri, S., Montori, A., Akikusa, N., Yamanshi, M., Giusfredi, G., Cancio, P., and De Natale, P. Comb-

- Assisted Subkilohertz Linewidth Quantum Cascade Laser for High-Precision Mid-Infrared Spectroscopy. *Applied Physics Letters*, 102(12):121117 (2013).
- [93] Cappelli, F., Galli, I., Borri, S., Giusfredi, G., Cancio, P., Mazzotti, D., Montori, A., Akikusa, N., Yamanishi, M., Bartalini, S., and De Natale, P. Subkilohertz Linewidth Room-Temperature Mid-Infrared Quantum Cascade Laser Using a Molecular Sub-Doppler Reference. *Optics Letters*, 37(23):4811–4813 (2012).
- [94] Hansen, M. G., Magoulakis, E., Chen, Q.-F., Ernsting, I., and Schiller, S. Quantum Cascade Laser-Based Mid-IR Frequency Metrology System with Ultra-Narrow Linewidth and 1×10^{-13} -Level Frequency Instability. *Optics Letters*, 40(10):2289 (2015).
- [95] Argence, B., Chanteau, B., Lopez, O., Nicolodi, D., Abgrall, M., Chardonnet, C., Daussy, C., Darquié, B., Le Coq, Y., and Amy-Klein, A. Quantum Cascade Laser Frequency Stabilization at the Sub-Hz Level. *Nature Photonics*, 9(7):456–460 (2015).
- [96] Sow, P. L. T., Mejri, S., Tokunaga, S. K., Lopez, O., Goncharov, A., Argence, B., Chardonnet, C., Amy-Klein, A., Daussy, C., and Darquié, B. A Widely Tunable 10- μm Quantum Cascade Laser Phase-Locked to a State-of-the-Art Mid-Infrared Reference for Precision Molecular Spectroscopy. *Applied Physics Letters*, 104(26):264101 (2014).
- [97] Schawlow, A. L. and Townes, C. H. Infrared and Optical Masers. *Physical Review*, 112(6):1940 (1958).
- [98] Henry, C. Theory of the Linewidth of Semiconductor Lasers. *IEEE Journal of Quantum Electronics*, 18(2):259–264 (1982).
- [99] Kikuchi, K. and Okoshi, T. Estimation of Linewidth Enhancement Factor of AlGaAs Lasers by Correlation Measurement between FM and AM Noises. *IEEE journal of quantum electronics*, 21(6):669–673 (1985).

- [100] Harder, C., Vahala, K., and Yariv, A. Measurement of the Line-width Enhancement Factor α of Semiconductor Lasers. *Applied Physics Letters*, 42(4):328–330 (1983).
- [101] Yu, Y., Giuliani, G., and Donati, S. Measurement of the Line-width Enhancement Factor of Semiconductor Lasers Based on the Optical Feedback Self-Mixing Effect. *IEEE Photonics Technology Letters*, 16(4):990–992 (2004).
- [102] Bartalini, S., Borri, S., Galli, I., Giusfredi, G., Mazzotti, D., Edamura, T., Akikusa, N., Yamanishi, M., and De Natale, P. Measuring Frequency Noise and Intrinsic Linewidth of a Room-Temperature DFB Quantum Cascade Laser. *Optics express*, 19(19):17996–18003 (2011).
- [103] Tombez, L., Schilt, S., Francesco, J., Führer, T., Rein, B., Walther, T., Domenico, G., Hofstetter, D., and Thomann, P. Linewidth of a Quantum-Cascade Laser Assessed from Its Frequency Noise Spectrum and Impact of the Current Driver. *Applied Physics B*, 109(3):407–414 (2012).
- [104] Tombez, L., Schilt, S., Di Francesco, J., Thomann, P., and Hofstetter, D. Temperature Dependence of the Frequency Noise in a Mid-IR DFB Quantum Cascade Laser from Cryogenic to Room Temperature. *Optics Express*, 20(7):6851–6859 (2012).
- [105] Orsal, B., Signoret, P., Peransin, J.-M., Daulasim, K., and Alabedra, R. Correlation between Electrical and Optical Photocurrent Noises in Semiconductor Laser Diodes. *IEEE Transactions on Electron Devices*, 41(11):2151–2161 (1994).
- [106] Guekos, G. and Strutt, M. Correlation Between Laser Emission Noise and Voltage Noise in GaAs CW Laser Diodes. *IEEE Journal of Quantum Electronics*, 5(2):129–130 (1969).
- [107] Myara, M., Signoret, P., Tourrenc, J.-P., Jacquet, J., Orsal, B. P., and Alabedra, R. M. Correlation between Tuning Section

- Electrical Noise and Optical Amplitude Fluctuations in DBR Two-and Three-Section Tunable Lasers Emitting around 1.55 μm . In *SPIE's First International Symposium on Fluctuations and Noise*, pages 246–256. International Society for Optics and Photonics (2003).
- [108] Dandridge, A. and Taylor, H. F. Correlation of Low-Frequency Intensity and Frequency Fluctuations in GaAlAs Lasers. *IEEE Journal of Quantum Electronics*, QE-18(10):1738–1750 (1982).
 - [109] Goobar, E., Karlsson, A., and Machida, S. Measurements and Theory of Correlation Between Terminal Electrical Noise and Optical Noise in a Two-Section Semiconductor Laser. *IEEE Journal of Quantum Electronics*, 29(2):386–395 (1993).
 - [110] Tombez, L. *Analysis and Improvement of the Spectral Properties in Mid-Infrared Semiconductor Quantum Cascade Lasers*. Ph.D. thesis, Université de Neuchâtel (2014).
 - [111] Schilt, S., Tombez, L., Tardy, C., Bismuto, A., Blaser, S., Maulini, R., Terazzi, R., Rochat, M., and Sudmeyer, T. An Experimental Study of Noise in Mid-Infrared Quantum Cascade Lasers of Different Designs. *Appl. Phys. B*, 119(1):189–201 (2015).
 - [112] Bartolo, R. E., Kirkendall, C. K., Kupershmidt, V., and Siala, S. Achieving Narrow Linewidth Low-Phase Noise External Cavity Semiconductor Lasers through the Reduction of 1/f Noise. In Mermelstein, C. and Bour, D. P., editors, *Proc. SPIE*, volume 6133, pages 61330I1–8 (2006).
 - [113] Yamanishi, M., Hirohata, T., Hayashi, S., Fujita, K., and Tanaka, K. Electrical Flicker-Noise Generated by Filling and Emptying of Impurity States in Injectors of Quantum-Cascade Lasers. *Journal of Applied Physics*, 116(18):183106 (2014).
 - [114] Chen, X.-y. *Lattice Scattering and 1/f Noise in Semiconductors*. Ph.D. thesis, Technische Universiteit Eindhoven (1997).

- [115] Blaser, S., Yarekha, D. A., Hvozdara, L., Bonetti, Y., Muller, A., Giovannini, M., and Faist, J. Room-Temperature, Continuous-Wave, Single-Mode Quantum-Cascade Lasers at $\lambda \simeq 5.4 \mu\text{m}$. *Applied Physics Letters*, 86(4):041109 (2005).
- [116] Vankwikelberge, P., Buytaert, F., Franchois, A., Baets, R., Kuindersma, P., and Fredriksz, C. Analysis of the Carrier-Induced FM Response of DFB Lasers: Theoretical and Experimental Case Studies. *IEEE Journal of Quantum Electronics*, 25(11):2239–2254 (1989).
- [117] Kobayashi, S., Yamamoto, Y., Ito, M., and Kimura, T. Direct Frequency Modulation in AlGaAs Semiconductor Lasers. *IEEE Journal of Quantum Electronics*, 18(4):582–595 (1982).
- [118] Gürel, K., Schilt, S., Bismuto, A., Bidaux, Y., Tardy, C., Blaser, S., Gresch, T., and Südmeyer, T. Frequency Tuning and Modulation of a Quantum Cascade Laser with an Integrated Resistive Heater. *Photonics*, 3(3):47 (2016).
- [119] Sackett, D. Supply Constant Power Level To A Varying Load Impedance. *Electronic Design* (2006).
- [120] Libbrecht, K. G. and Hall, J. L. A Low-Noise High-Speed Diode Laser Current Controller. *Review of Scientific Instruments*, 64(8):2133–2135 (1993).
- [121] Erickson, C. J., Van Zijll, M., Doermann, G., and Durfee, D. S. An Ultrahigh Stability, Low-Noise Laser Current Driver with Digital Control. *Review of Scientific Instruments*, 79(7):073107 (2008).
- [122] Troxel, D. L., Erickson, C. J., and Durfee, D. S. Note: Updates to an Ultra-Low Noise Laser Current Driver. *Review of Scientific Instruments*, 82(9):096101 (2011).

- [123] Seck, C. M., Martin, P. J., Cook, E. C., Odom, B. C., and Steck, D. A. Noise Reduction of a Libbrecht–Hall Style Current Driver. *Review of Scientific Instruments*, 87(6):064703 (2016).
- [124] Taubman, M. S. Low-Noise High-Performance Current Controllers for Quantum Cascade Lasers. *Review of Scientific Instruments*, 82(6):064704 (2011).
- [125] Biswas, A. and Basu, P. K. Equivalent Circuit Models of Quantum Cascade Lasers for SPICE Simulation of Steady State and Dynamic Responses. *Journal of Optics A: Pure and Applied Optics*, 9(1):26–32 (2007).
- [126] Chen, G. C., Fan, G. H., and Li, S. T. Spice Simulation of a Large-Signal Model for Quantum Cascade Laser. *Optical and Quantum Electronics*, 40(9):645–653 (2008).
- [127] Jung, W. G. and Marsh, R. Picking Capacitors. *Audio* (1980).
- [128] AD8429 1 nV/ $\sqrt{\text{Hz}}$ Low Noise Instrumentation Amplifier (2011).
- [129] Williams, J., editor. *The Art and Science of Analog Circuit Design*. EDN series for design engineers. Butterworth-Heinemann, Boston (1998). OCLC: 833247706.
- [130] LT1251 LT1256 40MHz Video Fader and DC Gain Controlled Amplifier (1994).
- [131] Wavelength Electronics QCL Series Low-Noise Quantum Cascade Laser Driver Datasheet And Operating Guide (2013).
- [132] Ginestar, S. *Fabrication and Characterisation of a Dual-Mode DFB Laser for Radio over Fibre Applications*. Ph.D. thesis, Université des Sciences et Technologie de Lille (2009).
- [133] Chan, S.-C., Hwang, S.-K., and Liu, J.-M. Radio-over-Fiber Transmission from an Optically Injected Semiconductor Laser

- in Period-One State. *Physics and Simulation of Optoelectronic Devices XV*, 6468:646811 (2007).
- [134] Martini, R. and Whittaker, E. Quantum Cascade Laser-Based Free Space Optical Communications. *Journal of Optical and Fiber Communications Reports*, 2(4):279–292 (2005).
- [135] Diaz, R., Chan, S.-C., and Liu, J.-M. Lidar Detection Using a Dual-Frequency Source. *Optics letters*, 31(24):3600–3602 (2006).
- [136] Sun, J., Dai, Y., Chen, X., Zhang, Y., and Xie, S. Stable Dual-Wavelength DFB Fiber Laser With Separate Resonant Cavities and Its Application in Tunable Microwave Generation. *IEEE Photonics Technology Letters*, 18(24):2587–2589 (2006).
- [137] Carpintero, G., Rouvalis, E., Lawniczuk, K., Fice, M., Renaud, C. C., Leijtens, X. J., Bente, E. A., Chitoui, M., Van Dijk, F., and Seeds, A. J. 95 GHz Millimeter Wave Signal Generation Using an Arrayed Waveguide Grating Dual Wavelength Semiconductor Laser. *Optics Letters*, 37(17):3657–3659 (2012).
- [138] Calvar, A., Amanti, M. I., Renaudat St-Jean, M., Barbieri, S., Bismuto, A., Gini, E., Beck, M., Faist, J., and Sirtori, C. High Frequency Modulation of Mid-Infrared Quantum Cascade Lasers Embedded into Microstrip Line. *Applied Physics Letters*, 102(18):181114 (2013).
- [139] Chen, G., Bethea, C. G., Martini, R., Grant, P. D., Dudek, R., and Liu, H. C. High-Speed All-Optical Modulation of a Standard Quantum Cascade Laser by Front Facet Illumination. *Applied Physics Letters*, 95(10):101104 (2009).
- [140] Cathabard, O., Teissier, R., Devenson, J., and Baranov, A. N. InAs-Based Distributed Feedback Quantum Cascade Lasers. *Electronics Letters*, 45(20) (2009).

- [141] Wittmann, A., Bonetti, Y., Fischer, M., Faist, J., Blaser, S., and Gini, E. Distributed-Feedback Quantum-Cascade Lasers at 9 μm Operating in Continuous Wave Up to 423 K. *IEEE Photonics Technology Letters*, 21(12):814–816 (2009).
- [142] Sadeghi, A., Liu, P. Q., Wang, X., Fan, J., Troccoli, M., and Gmachl, C. F. Wavelength Selection and Spectral Narrowing of Distributed Bragg Reflector Quantum Cascade Lasers up to Peak Optical Power. *Optics Express*, 21(25):31012–31018 (2013).
- [143] Orfanidis, S. J. *Electromagnetic Waves and Antennas*. Rutgers University (2016).
- [144] Villares, G., Hugi, A., Blaser, S., and Faist, J. Dual-Comb Spectroscopy Based on Quantum-Cascade-Laser Frequency Combs. *Nature Communications*, 5:5192 (2014).
- [145] Bismuto, A., Bidaux, Y., Blaser, S., Terazzi, R., Gresch, T., Rochat, M., Muller, A., Bonzon, C., and Faist, J. High Power and Single Mode Quantum Cascade Lasers. *Optics Express*, 24(10):10694–10699 (2016).
- [146] Villanueva, G. E., Perez-Millan, P., Palaci, J., Cruz, J. L., Andres, M. V., and Marti, J. Dual-Wavelength DFB Erbium-Doped Fiber Laser With Tunable Wavelength Spacing. *IEEE Photonics Technology Letters*, 22(4):254–256 (2010).
- [147] Blanchard, R., Menzel, S., Pfügl, C., Diehl, L., Wang, C., Huang, Y., Ryou, J.-H., Dupuis, R. D., Dal Negro, L., and Capasso, F. Gratings with an Aperiodic Basis: Single-Mode Emission in Multi-Wavelength Lasers. *New Journal of Physics*, 13(11):113023 (2011).
- [148] Süess, M. J., Wolf, J. M., Jouy, P., Bonzon, C., Beck, M., Hundt, M., Tuzson, B., Emmenegger, L., and Faist, J. Analysis of Dual-Section DFB-QCLs for Spectroscopic Applications.

- In *Compound Semiconductor Week (CSW) [Includes 28th International Conference on Indium Phosphide & Related Materials (IPRM) & 43rd International Symposium on Compound Semiconductors (ISCS), 2016]*, pages 1–2. IEEE (2016).
- [149] St-Jean, M. R., Amanti, M. I., Bernard, A., Calvar, A., Bismuto, A., Gini, E., Beck, M., Faist, J., Liu, H. C., and Sirtori, C. Injection Locking of Mid-Infrared Quantum Cascade Laser at 14 GHz, by Direct Microwave Modulation: Injection Locking of Mid-Infrared Quantum Cascade Laser. *Laser & Photonics Reviews*, 8(3):443–449 (2014).
 - [150] St-Jean, M. R., Amanti, M., Bismuto, A., Beck, M., Faist, J., and Sirtori, C. Mode Stabilization in Quantum Cascade Lasers via an Intra-Cavity Cascaded Nonlinearity. *Optics Express*, 25(3):1847 (2017).
 - [151] Hugi, A. *Single-Mode and Comb Operation of Broadband QCLs*. Ph.D. thesis, ETH Zurich (2013).
 - [152] Cappelli, F., Villares, G., Riedi, S., and Faist, J. Intrinsic Line-width of Quantum Cascade Laser Frequency Combs. *Optica*, 2(10):836–840 (2015).
 - [153] Gross, M. C., Callahan, P. T., and Dennis, M. L. A Fiber Laser Photonic Frequency Synthesizer: Concept, Performance, and Applications. *Johns Hopkins APL Technical Digest*, 30(4):287–298 (2012).
 - [154] Liang, W., Eliyahu, D., Ilchenko, V. S., Savchenkov, A. A., Matsko, A. B., Seidel, D., and Maleki, L. High Spectral Purity Kerr Frequency Comb Radio Frequency Photonic Oscillator. *Nature Communications*, 6:7957 (2015).
 - [155] Faist, J., Hugi, A., and Villares, G. Method and Device for Frequency Control and Stabilization of a Semiconductor Laser (2015).

- [156] Sergachev, I., Maulini, R., Bismuto, A., Blaser, S., Gresch, T., and Muller, A. Gain-Guided Broad Area Quantum Cascade Lasers Emitting 23.5 W Peak Power at Room Temperature. *Optics Express*, 24(17):19063 (2016).
- [157] High Peak Power Source. <http://www.alpeslasers.ch/?a=28,126,180> (2017).
- [158] Starter Kit. <http://www.alpeslasers.ch/?a=28,35,171> (2017).
- [159] Sergachev, I., Maulini, R., Bismuto, A., Blaser, S., Gresch, T., Bidaux, Y., Müller, A., Schilt, S., and Südmeyer, T. All-Electrical Frequency Noise Reduction and Linewidth Narrowing in Quantum Cascade Lasers. *Optics Letters*, 39(22):6411 (2014).
- [160] Fischer, M., Tuzson, B., Hugi, A., Brönnimann, R., Kunz, A., Blaser, S., Rochat, M., Landry, O., Müller, A., and Emmenegger, L. Intermittent Operation of QC-Lasers for Mid-IR Spectroscopy with Low Heat Dissipation: Tuning Characteristics and Driving Electronics. *Optics Express*, 22(6):7014 (2014).

A

Probe for RF measurements

A RF probe in a shape of a press-contact together with an adapted laser housing have been fabricated in order to measure weak RF beatnotes from Fabry-Perot, comb and DBR QCLs on standard copper mounts (Figure A.1). The probe consists of a small two-side PCB with a piece of copper soldered on one side slightly hanging off; a standard coaxial cable has been soldered to it, being glued with epoxy on its other connectorized side to the package lid (Figure A.2). The latter has allowed to combine the setup with a fore-vacuum pump, in order to perform measurements at negative temperatures without having water condensations on the laser chip.

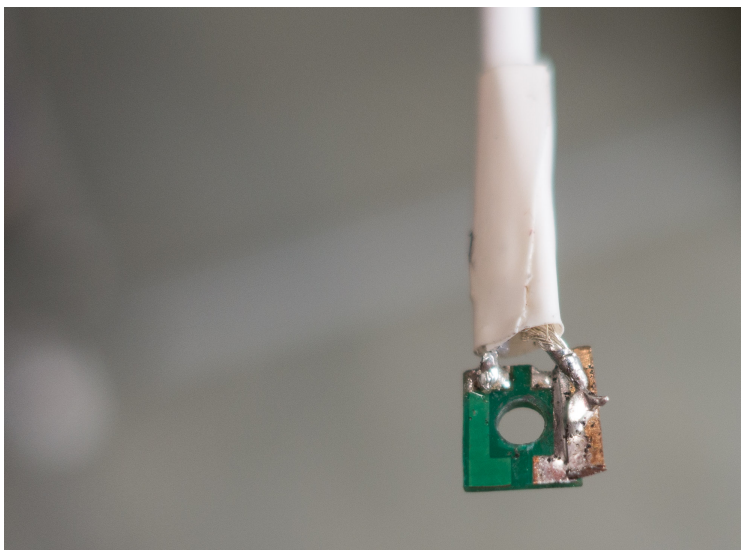


Figure A.1: Tip of RF press-contact probe for QCLs on a standard chip on carrier type submount. The minimal distance between coaxial cable and laser under test allows successfully peaking up the weak measured signals.

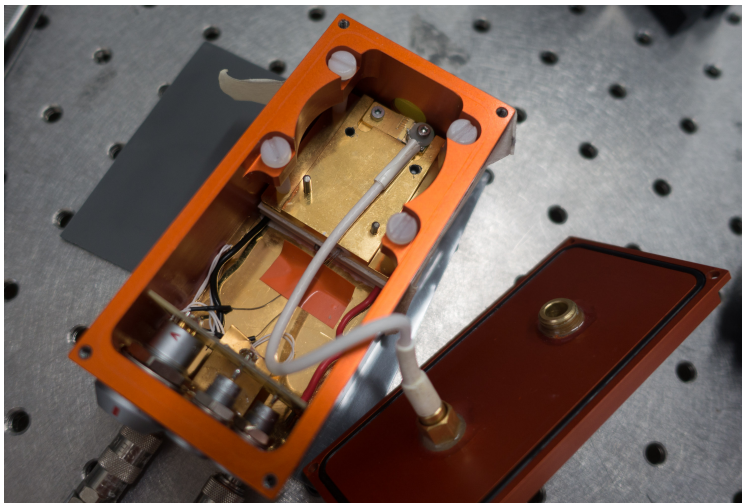


Figure A.2: Standard LLH for QCLs modified for RF measurements. The white coaxial cable is used both for driving the laser and measuring its electrical beatnote.

B

Measurement of frequency tuning

Laser frequency tuning is its important characteristic for spectroscopic applications. During this work, an *Intermittent Continuous Wave* (ICW) driver [160] has been used to measure frequency tuning of certain single-mode QCLs during current pulses. If a low finesse etalon is placed in front of the laser under test, and light is then registered with an optical detector, counting fringes in the resulting signal allows measuring precisely the relative change of optical frequency Figure B.1. Another important application of such a setup is checking for absence of mode hops and spectral purity, as any of those result in the discontinuous tuning curve.

The driver has been modified in terms of hardware and software from the state it was manufactured by EMPA in order to facilitate output current measurements and improve its user interface.

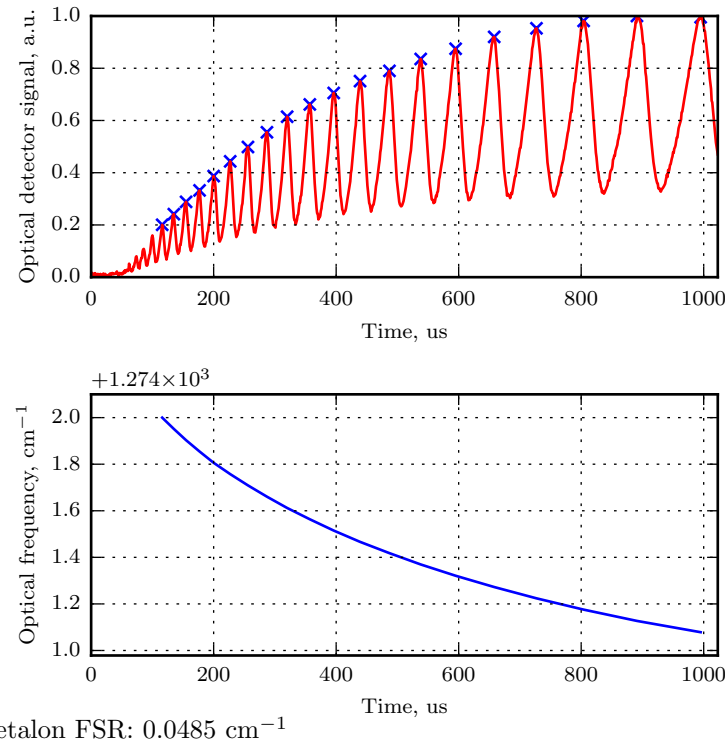


Figure B.1: Top: recorded signal of 1 ms pulse of a 7.8 μm DFB QCL passed through a low finesse optical etalon. Bottom: frequency tuning curve derived from the upper plot.

C

Beam collimation

Care has to be taken when collimating a QCL beam: due to sufficient beam divergence (40-60 degrees FWHM) a high numerical aperture lens has to be used in order to collect light efficiently and introduce a minimal distortion. Otherwise major problems can be faced because of the beam cropping (Figure C.1).

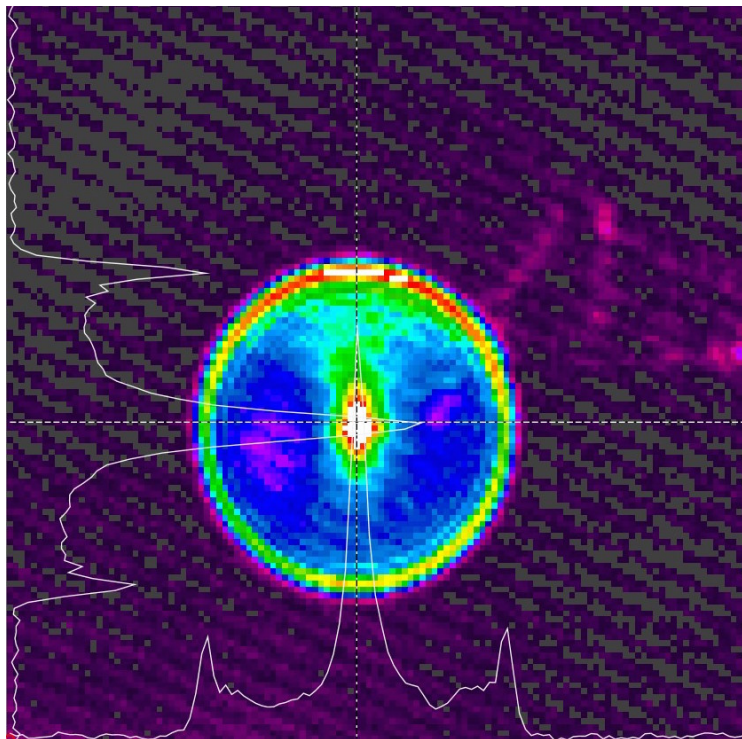


Figure C.1: False color QCL beam intensity profile distorted by $d=12$ mm window of a standard LLH package, collimated with $f=25.4$ mm lens.



Tools

Highlights of open source and closed source free instruments and resources used during this work:

- Linux OS:
<https://www.kernel.org/>
- L^AT_EX document preparation system:
<https://www.latex-project.org/>
- Git version control system:
<https://git-scm.com/>
- Zotero research source organization tool:
<https://www.zotero.org/>
- Gummi – L^AT_EX editor with live preview,
<https://github.com/alexandervdm/gummi>
- SmartGit – a visual client for git,
<https://www.synteko.com/smartygit/>
- Qt cross-platform application framework,
<https://www.qt.io>

- CLion, IDE for C and C++:
<https://www.jetbrains.com/clion/>
- PyCharm, IDE for Python:
<https://www.jetbrains.com/pycharm/>
- Jupyter Notebook:
<https://jupyter.org/>
- matplotlib plotting library:
<https://matplotlib.org/>
- pyqtgraph plotting library:
<http://www.pyqtgraph.org/>
- numpy package for scientific computing:
<http://www.numpy.org/>
- scipy library for scientific computing:
<https://www.scipy.org/>
- python-ivi, a python library implementing communication with scientific equipment:
<https://github.com/python-ivi/python-ivi>
- MyHDL, python package for HDL design and simulation:
<http://www.myhdl.org/>
- GaussianBeam, Gaussian optics simulator:
<http://gaussianbeam.sourceforge.net/>
- ComponentLibrary, a vector graphics library for illustrations of optics experiments:
<https://www.gwoptics.org/ComponentLibrary/>
- LTSpice, SPICE simulator of electronic circuits:
<http://www.linear.com/design-tools/software/#LTspice>
- KiCad EDA, A Cross Platform and Open Source Electronics Design Automation Suite:
<http://kicad-pcb.org/>

- Red Pitaya Notes, a collection of open source solutions for Red Pitaya boards:
<https://pavel-demin.github.io/red-pitaya-notes/>
- LightMachinery Optical Design Tools:
<https://lightmachinery.com/optical-design-center/>
- HITRAN on the Web:
<http://hitran.iao.ru/>
- Refractive index database:
<https://refractiveindex.info/>
- L^AT_EX template used for this document (slightly modified):
<https://github.com/ivangiangreco/basilea-latex>
- latexdiff, a tool to determine and mark up significant differences between L^AT_EX files:
<https://www.ctan.org/pkg/latexdiff>